Article:

Developing a Predictive Model for Low Temperature Laval Nozzles with Applications in Chemical Kinetics

L. Driver,[1] K. Douglas,[2] D.I. Lucas,[3] T. Guillaume,[4] J.H. Lehman,[3] N. Kapur,[5] D.E. Heard,[2] and G.N de Boer[5]

[1]*School of Computing, University of Leeds, EPSRC CDT in Fluid Dynamics, United Kingdom, Woodhouse Lane, LS2 9JT*

[2]*School of Chemistry, University of Leeds, United Kingdom, LS2 9JT*

[3]*School of Chemistry, University of Birmingham, Edgbaston, United Kingdom, B15 2TT*

[4]*LOMA, Université de Bordeaux, CNRS, UMR 5798, Talence Cedex, F-33405, 351 cours de la Libération, France*

[5]*School of Mechanical Engineering, University of Leeds, United Kingdom, LS2 9JT*

(*Electronic mail: scldr@leeds.ac.uk)

(Dated: 5 July 2024)

Laval nozzles are used in the CRESU ("Cinétique de Réaction en Écoulement Supersonique Uniforme") method to generate a collimated low temperature (5 - 200K), low pressure (30 - 500 Pa), high Mach number (1 < M < 20) supersonic jet. Laval nozzles have been designed using the Method of Characteristics (MOC) since the development of CRESU, which is an analytical method that assumes inviscid, isentropic flow, and is routinely used to design nozzle profiles for a particular gas and temperature with a uniform shock free exit. This study aims to provide a robust computational framework to overcome the limitations of the MOC, whilst also providing recommendations on the numerical model setup required to model a low temperature supersonic jet. It also discusses the blockage effects when using the Pitot tube method for flow characterisation, the influence of inlet turbulence and reservoir size. Numerical results are validated using two different experimental apparatuses from research groups at the University of Leeds and the University of Birmingham. Lastly, a MATLAB framework was developed and has been provided as an open source toolbox to allow any user to perform Computational Fluid Dynamics (CFD) on any Laval nozzle, with the ability to change nozzle geometry, operating conditions and bath gas. The toolbox has been rigorously tested against many benchmark cases, which shows that steady-state Reynolds Averaged Navier Stokes (RANS) with the k-omega-Shear Stress Transport (k-ω-SST) turbulence model can be used to accurately predict global quantities, such as average temperature in the stable region of the supersonic jet.

I. INTRODUCTION

Low-temperature kinetics of chemical reactions can demonstrate non-Arrhenius behaviour[1–4], for example due to quantum mechanical tunnelling through a barrier to reaction, and can have relatively large rate coefficients (on the order of 10^{-11} cm^3 molecule^{-1} s^{-1}). Such reactions can contribute substantially to the chemistry within the interstellar medium (ISM). The ISM is the space between stars and consists almost entirely of gas (99% by mass - with dust making up the balance)[1]. The formation of complex organic molecules through the reactions taking place in the ISM is of interest as they could be involved in early prebiotic biochemical reactions, potential precursors to ribonucleotides, phospholipids, sugars, amino acids and subsequently impact our understanding of the origin of life[5–7]. A common approach in the study of low-temperature gas phase reactions is the CRESU ("Cinétique de Réaction en Écoulement Supersonique Uniforme") method which at its heart employs a Laval nozzle to recreate the low-temperature conditions of the ISM and allows kinetic measurements of gas phase reactions to be studied in the laboratory[8–12]. Analytical methods are routinely used to design an axisymmetric Laval nozzle[11,13], although due to inherent assumptions within such models, such as isentropic, and inviscid flow, these methods struggle to accurately predict important flow features of the supersonic jet. These features include (i) the stable flow length, which is dependent on the rate at which the turbulence mixing layer that surrounds the isentropic core propagates downstream, and (ii) temperature variation across the jet, which is dependent on the generation of shockwaves and their interaction with the boundary layer.

Computational Fluid Dynamics (CFD) offers a high-fidelity numerical approach which resolves viscous effects, and can provide accurate information about the flow length and temperature variations for any nozzle profile, whilst also providing a platform that allows unrestricted experimentation. Although some groups adopt CFD to support the design of their nozzles[14], this is not universal across CRESU groups worldwide, and the accuracy of such models remains unexplored. A further opportunity would also be to develop a toolkit, providing the wider community access to robust CFD models, allowing rapid predictions of supersonic jets for a variety of nozzle shapes, chamber sizes and operating conditions to be carried out and further reducing experimental validation.

The work carried out in this study validates the use of CFD for characterising low temperature, low pressure, supersonic wakes, and describes an automated computational framework for supersonic nozzles. The automation framework can be used by the CRESU community, and others, that may want to automate their own systems using a similar approach to that detailed in this study. By understanding nozzle flows and temperature variations, more accurate kinetic measurements can be made. Nozzles can potentially be designed for a specific target temperature, which would aid in capturing the full temperature range for low-temperature kinetic laboratory experiments.
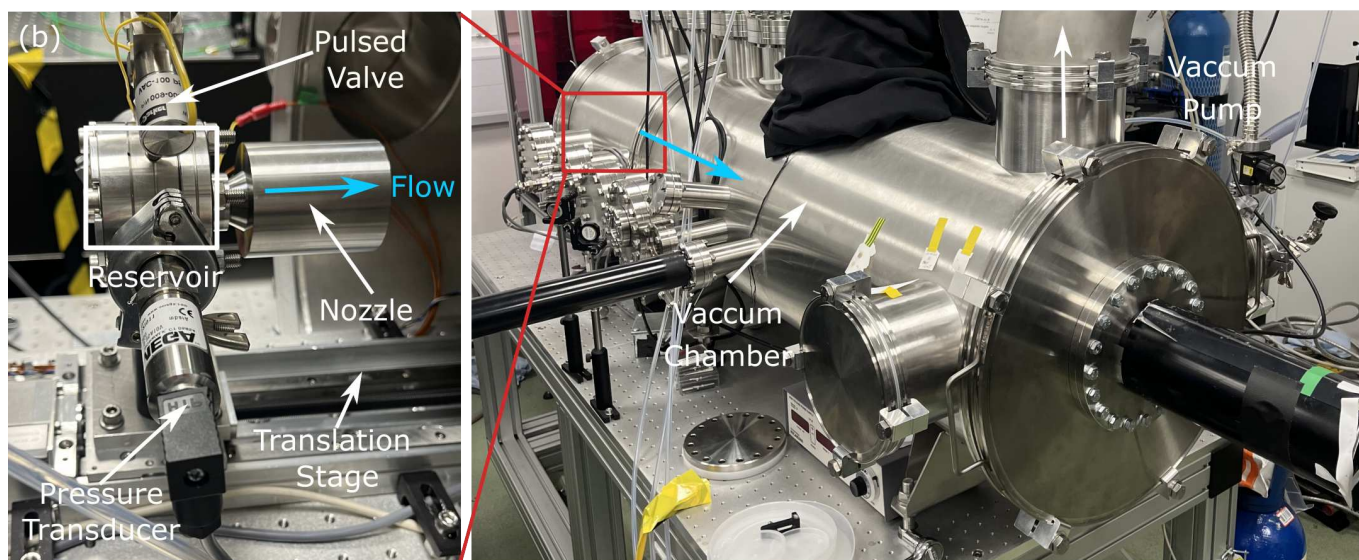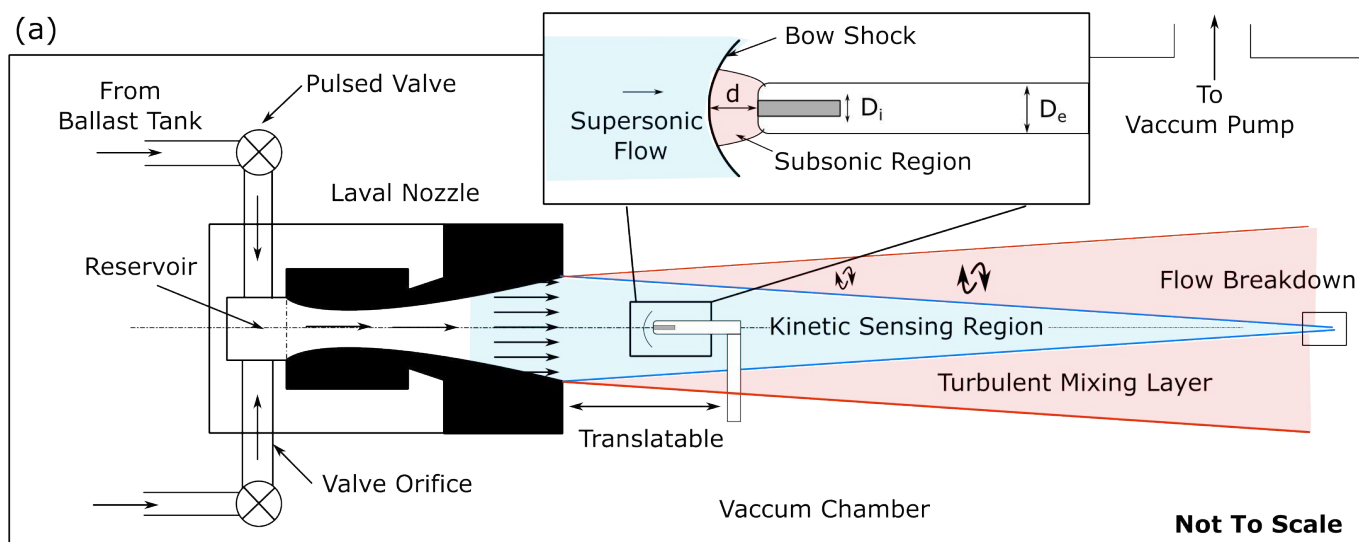
FIG. 1. Cross-sectional schematic (top) showing the internals of a pulsed CRESU system, which shows the Laval nozzle generating a collimated supersonic flow, where the cold isentropic core region is used to perform chemical kinetic measurements. It also illustrates how the Pitot tube technique is used for impact pressure measurements to characterise jet performance. Blue and red shaded areas indicate regions of low temperature and high temperature (≈ 300 K) respectively. The zoomed-in picture of the Pitot tube shows the bow shock that forms at the leading edge of the Pitot tube. Picture of the CRESU apparatus at the Univeristy of Birmingham (bottom), labels relate to what is seen in the schematic.

A. The CRESU Method

The CRESU method was developed in the 1980s by Rowe and co-workers to study ion molecule reactions, and later to study neutral-neutral reactions[15]. The CRESU method addresses the drawbacks of (i) cryogenic cooling within a vessel, which suffers from reagent condensation on the surrounding walls, and (ii) free expansion flows using a pinhole nozzle where large anisotropies in temperature are present in the jet due to strong shockwave features[2,15]. Designs of the CRESU apparatus were originally based on continuous flow, although there have been several advancements, notably to the pulsed inlet developed by Atkinson and Smith in 1995[11] and the pulsed inlet based on an aerodynamic chopper by Jimenez et al., in 2015[12]. The advancement to the pulsed system has subsequently decreased apparatus size and pumping capacity requirements, allowing more groups to utilise the approach[2,12,16]. The pulsed configuration has been shown to achieve similar results to continuous operation with the same nozzle, bath gas and pressure conditions[2]. The lowest temperature recorded in the literature to date using the continuous CRESU method was 5.8 K in 2010 by Berteloitte et al.,[17]. This was achieved using a continuous gas flow and precooling the reservoir to 77 K using liquid nitrogen. A schematic

of the pulsed CRESU setup, together with a photograph of a typical laboratory apparatus is shown in Figure 1.

Laval nozzles used in the CRESU method are designed exclusively using the Method of Characteristics (MOC) with an additional boundary layer (BL) adaptation[9,11,13,18,19]. Nozzles are designed specifically for one temperature, mass flow rate, bath gas and nozzle pressure ratio (NPR, which is the ratio between the inlet and exit pressure of the nozzle), hence an assortment of nozzles are required to perform low-temperature kinetics between 0 - 300 K. There have been attempts to improve the range of experiments that can be performed using one nozzle profile. Canosa et al.,[9] adapted the MOC and showed that the same nozzle profile can be used with different mixtures of gasses and pressures, which allows one nozzle to operate at a variety of temperatures. The MOC is a way to solve the irrotational, inviscid potential equations for supersonic flow to obtain a nozzle geometry that only ensures a uniform shock-free exit flow. This method generates a flow solution that does not resolve the viscous mixing layer that surrounds the isentropic core. Therefore the BL development across the nozzle is calculated and the profile of the nozzle is adjusted to account for this thickness.

The MOC fails to give any insight into (i) the length of the flow, which is controlled by the downstream development of the turbulent boundary layer that surrounds the stable core region, this determines both the residence time of the reaction species in the jet and which reactions can be studied and (ii) the magnitude of the shock structures which cause variations in the jet temperature. This is important as large variations in jet temperature contribute to errors in the kinetic rate coefficients that are measured. Fundamentally this method requires the designed nozzle to be manufactured and tested before its true performance can be determined. Commonly, the nozzle geometry and design conditions calculated using the MOC may be sub-optimal, and time-consuming experimental optimisation of conditions (i.e. by varying pressures) or a complete redesign of nozzle geometry has to be carried out. The use of a high-fidelity numerical model that accounts for viscous effects will improve flow prediction. With the exponential increase in computational power, CFD can be used to predict nozzle performance and can also be used as an intermediate prototyping step before manufacturing nozzles and testing them using experimental jet characterisation.

B. Experimental Jet Characterisation via Pitot Tubes

Experimentally, the jet downstream of the nozzle exit is most commonly characterised using the Pitot tube technique[20–23]. In a supersonic flow, a Pitot tube is used to measure the impact pressure at point-wise locations across the jet wake. The Mach number at each location is calculated using the Rayleigh-Pitot equation:

$$\frac{P_{impact}}{P_{res}} = \left(\frac{(\gamma+1)M^2}{(\gamma-1)M^2+2} \right)^{\frac{\gamma}{\gamma-1}} \left(\frac{\gamma+1}{2\gamma M^2-\gamma+1} \right)^{\frac{1}{\gamma-1}} \quad (1)$$

where P_{impact} is the impact pressure, obtained experimentally via a Pitot tube, P_{res} is the reservoir pressure, $\gamma = c_p/c_v$, is the ratio of specific heat capacities of the bath gases ($\gamma = 5/3$ and $\gamma = 1.4$ for monatomic and diatomic gases, respectively) and M is the Mach number. The adiabatic relationships can then be used to determine macroscopic flow properties, such as temperature, density and pressure. This method can be used to produce both 1D axial characterisation profiles and 2D contours of the jet, and is used by various groups to determine the quality and length of the supersonic jet[2,9,22,23].

Producing a 2D plot experimentally can take a significant quantity of time and resources, requiring a manufactured nozzle and sufficient bath gases. This method gives no information about many important jet properties, such as turbulent kinetic energy and vorticity. These can be obtained using numerical techniques to accurately predict turbulent mixing layer development and flow length.

As the Rayleigh-Pitot equation assumes 1D compressible, isentropic, inviscid and irrotational flow, the use of the equation outside the supersonic core and in the turbulent mixing layer is invalid. This can lead to a non-physical representation of the temperature in the mixing layer which surrounds the isentropic core[24,25]. Using this equation with impact pressure measurements in the mixing layer causes the temperature to tend towards absolute zero, which is not representative of what is happening in reality.

In the pulsed CRESU apparatus it is often very hard experimentally to measure flow conditions inside the nozzle and reservoir as the Pitot tube is either larger than the nozzle exit or the mount the Pitot tube is attached to prevents the movement into the nozzle. It is possible to use the Pitot tube to obtain flow parameters inside the nozzle if the diameter of the nozzle diameter is large or the Pitot diameter is small, although the Pitot tube method and analytical equations are invalid in the converging section and reservoir as the flow is subsonic. The majority of groups do not typically characterise the flow inside their reservoir or nozzle, therefore experimental flow profiles are only shown from the nozzle exit in the literature.

Furthermore, the inclusion of a blockage such as a Pitot tube can cause errors in experimental measurements due to the presence of a bow shock that forms at the Pitot leading edge. The extent of this phenomenon is highly dependent on the Pitot tube diameter in comparison to the nozzle exit, speed of the flow and location of the Pitot tube in the flow and has been shown experimentally and numerically by a variety of authors[26–28]. There is limited numerical research on the effect of a Pitot tube in a low-pressure supersonic jet produced by a Laval nozzle at high nozzle pressure ratios. These conditions are of interest as they are routinely used to perform flow characterisation. Therefore the blockage effect needs to be quantified as it may be affecting the accuracy of the flow measurements and in turn the accuracy of kinetic measurements.

C. Modelling Supersonic Nozzle Flow

Numerical investigation of supersonic jet wake dynamics generated by a Laval nozzle has been carried out by several authors. Balabel et al.,[29] discussed the impacts of turbulence models on flow predictions, concluding that the k-omega-Shear Stress Transport (k-ω SST) model provides the best comparisons to experiments in terms of capturing large flow gradients caused by shockwaves and the location of flow separation on the nozzle wall. The accuracy of the k-ω-SST model has similarly been confirmed and used by various authors to model supersonic and hypersonic flow in a variety of application areas[30–35]. The validation of a numerical model with experiments is typically achieved by comparing the pressure across the nozzle wall. These studies show that turbulence models can accurately predict flow variables inside the nozzle and on the walls[32]. This is then used to infer that the supersonic jet is performing as intended, which is not necessarily true. Many studies use Reynolds Average Navier Stokes (RANS) models and compare numerical and experimental results of the jet structure and flow quantities past the nozzle exit. The RANS models that are used can struggle to accurately predict the point-wise structure of the jet, although they can be used to obtain global quantities of interest, such as flow rate and entrainment ratio[33,35–37]. Large Eddy Simulations (LES) have been performed on Laval nozzles, for example, Munday et al.,[38] compares LES results to experimental data and showed excellent agreement of supersonic jet structure and point-wise quantities such as velocity. Therefore this study would provide insight into whether RANS models could be used to predict global temperatures of supersonic wakes for use within chemical kinetic studies.

Some groups performing low-temperature kinetics have carried out CFD calculations on their nozzles, although the information provided on the computational methods and the comparison of CFD and experimental results is very limited[25,39,40]. Generally, the agreement between experimental and computational results is relatively poor and may be a result of model specification.

Suas-David et al.,[25] compared steady-state freestream CFD calculations with experimental Pitot tube measurements of a pulsed CRESU system, which showed that the diameter of the isentropic core predicted by the CFD decays substantially quicker than the experiments. They suggested the discrepancy was due to the steady-state pressure inlet used in the CFD to model the pulsed nature of the flow, although this was not investigated in detail.

Thawoos et al.,[39] used CFD to evaluate nozzle performance at various NPR's and compared it to experimental measurements using resonance-enhanced multiphoton ionization. The CFD shows good agreement with global parameters across the supersonic jet, i.e. average temperature, but struggles to predict the point-wise solution of the axial Mach number and static temperature profiles.

Abdelkader Khedaoui[14] also performed CFD on low temperature supersonic nozzles which were used in the CRESU method, again no turbulence model was specified, and detailed that it took 20 days to setup and perform CFD on one nozzle geometry.

Laval nozzles are frequently researched and there have been various numerical studies comparing CFD results to experiments. However, there has not been a full-scale CFD investigation into the effects that turbulence models, discretisation schemes, boundary conditions, chamber sizes, and reservoir sizes have on the jet quality and structure in regard to the CRESU method. Performing this structured analysis will provide insight into how the numerical model responds to varying inputs and the effect this has on the validity of numerical predictions at low temperatures and pressures. There are commercial tools, such as Ansys and OpenFOAM that have been used to aid nozzle characterisation although users will have to manually set up the geometry, mesh and solution for each case that is of interest. Therefore the work presented here will also aim to develop an automated predictive tool that is integrated with commercial software, which automates the CFD workflow, allowing chemical researchers to use CFD to rapidly prototype nozzles made using existing design methods such as the MOC.

Following the aforementioned motivations, the goal of this study is to introduce a multidisciplinary approach to improve the current state of the art of flow characterisation and provide a means of rapid prototyping in the CRESU method, and this will be achieved through:

1. A combined experimental and computational study of a benchmark nozzle, which explores the physics of high Mach number, low Reynolds number flows used for the study of reaction kinetics in the pulsed CRESU apparatus.

2. Extending the CFD framework to analyse its prediction performance with a range of existing nozzles and design conditions.

3. Providing a computational framework that automates the entire CFD workflow. This framework will aim to allow users to input any nozzle profile, chamber size, reservoir size and inlet condition and receive high-fidelity CFD data without needing prior CFD knowledge.

The remainder of the paper is structured as follows, Section II provides the necessary background to isentropic flow theory, which will be used in interpreting the results. Section III A 1 and III A 2 summarises the Laval nozzles used and experimental apparatus respectively, and Section III B outlines the numerical methodology. Section IV is the results section, which describes results from tests performed on a benchmark nozzle. Section V provides information on the development of the automated CFD framework. Finally, Section VI uses the computational framework on a variety of nozzles, with varying pressure and bath gases for experimental comparison. This final section demonstrates the capability of this newly developed approach and the benefits it brings to the field.

II. BACKGROUND

A. Laval Nozzle Theory

The Laval nozzle has three distinct features, the converging section, the throat and the diverging section as shown in Figure 1. A relationship between the Mach number and nozzle area can be found by enforcing mass conservation and assuming a quasi-1D, isentropic, inviscid flow[41]:

$$(1-M^2)\frac{du}{u} = -\frac{dA}{A},\tag{2}$$

where A is the area along the 1D length and M is the Mach number, which is a dimensionless quantity found by normalising the fluid velocity (u) with the sound speed (c). The speed of sound is only dependent on fluid temperature and can be calculated with $c = \sqrt{\gamma r T}$, where γ is the specific heat ratio, r is the specific gas constant and T is temperature.

In the converging section where $dA < 0$, gas accelerates from subsonic ($M < 1$) to transonic ($M = 1$). The throat is defined as the section where $dA = 0$, and so by necessity, the Mach number has to equal unity at the throat, known as the sonic point. The sonic point is critical to ensure the diverging section accelerates the flow. When $M > 1$, $(1-M^2)$ becomes negative and hence the flow can be accelerated from transonic to supersonic ($M > 1$) when $dA > 0$. During the transformation from subsonic to supersonic thermal energy is converted to kinetic energy, decreasing flow temperature substantially. An analytical relationship between nozzle area ratio and Mach number in the diverging section is given by:

$$\frac{A}{A^*} = \left(\frac{\gamma+1}{2}\right)^{-\frac{\gamma+1}{2(\gamma-1)}} \frac{\left(1+\frac{\gamma-1}{2}M^2\right)^{\frac{\gamma+1}{2(\gamma-1)}}}{M}\tag{3}$$

where A is the local nozzle area and A^* is the nozzle throat area. The temperature, pressure and density of the flow can be determined from the Mach number using the following isentropic relationships:

$$\frac{T_{flow}}{T_{res}} = \left(1+\frac{\gamma-1}{2}M^2\right)^{-1},\tag{4}$$

$$\frac{\rho_{flow}}{\rho_{res}} = \left(1+\frac{\gamma-1}{2}M^2\right)^{\frac{-1}{\gamma-1}},\tag{5}$$

$$\frac{P_{flow}}{P_{res}} = \left(1+\frac{\gamma-1}{2}M^2\right)^{\frac{-\gamma}{\gamma-1}},\tag{6}$$

where T_{flow} and T_{res} is the flow and reservoir temperature respectively, ρ_{flow} and ρ_{res} is the flow and reservoir density respectively, and P_{flow} and P_{res} is the flow and reservoir pressure respectively. These can be used with existing nozzles to estimate the pressure required to obtain an optimal flow. The angle of the shockwave that propagates from the nozzle exit can be calculated using the Prandtl-Meyer equation:

$$v = \sqrt{\frac{\gamma+1}{\gamma-1}}tan^{-1}\sqrt{\frac{\gamma-1}{\gamma+1}(M^2-1)} - tan^{-1}\sqrt{(M^2-1)},\tag{7}$$

where v is the shockwave angle, and it solely depends on the Mach number and ratio of specific heat capacity of the gas. Equation 7 will be used for additional validation of the shockwave structures that form in the numerical study. The flow characteristics of a supersonic nozzle wake, are determined by the nozzle pressure ratio (NPR), which is defined as the ratio between the nozzle inlet pressure and the outlet, the nozzle geometry and the gas used i.e. monatomic or diatomic[10,18,42]. Shockwaves are only generated when pressure waves exceed the local speed of sound, this causes a discontinuity, an irreversible sharp change in local macroscopic quantities, such as temperature and velocity[41]. 1D Nozzle theory gives fast approximations for jet properties in the isentropic core, although it doesn't consider 3D effects, viscosity or turbulence.

B. Flow Regimes

There are a variety of flow regimes that can occur in a supersonic Laval nozzle. These regimes are important in the context of chemical kinetics as they can affect the temperature in the wake region where kinetics are carried out. Flow regimes are dependent on the upstream reservoir pressure (P_{res}), the ambient pressure (P_{amb}), which is the pressure in the chamber far away from the flow, and the pressure at the nozzle exit (P_{exit})[43]. Figure 2 shows how increasing the pressure between P_{amb} and P_{res} (i.e. keeping P_{res} constant and reducing P_{amb}) changes the flow regimes and affects temperature across the nozzle and supersonic jet.
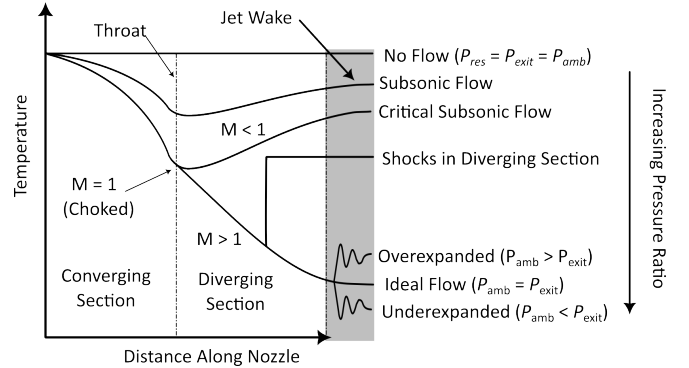
FIG. 2. Effect of flow regime on temperature profile across the nozzle length and in the region downstream from the nozzle exit. The jet wake is indicated by the grey shaded region and inside the nozzle is indicated by the white region. M is the Mach number. P_{amb} is the ambient pressure, P_{exit} is nozzle exit pressure and P_{res} is reservoir pressure.

No flow occurs when $P_{res} = P_{exit} = P_{amb}$, this is where the flow is stagnant as there is no pressure driving the flow. The subsonic regime occurs when the flow has not reached the sonic point ($M = 1$) at the throat, therefore the diverging section acts to reduce the flow speed as discussed in section II A. In the critical subsonic regime, the flow is choked (i.e. mass flow remains constant) as the flow speed is equal to the sonic point at the throat. Once the flow is choked, reducing the ambient pressure has no affect mass flow through the nozzle[43].

As the pressure ratio is not large enough, flow speed and temperature return to subsonic conditions. At this point, any reduction in pressure ratio will return the nozzle to subsonic conditions. If the pressure ratio is increased just past the critical subsonic regime, a normal shock will develop in the diverging section of the nozzle. Across the normal shock, a large change in temperature occurs and the flow returns to subsonic. Shockwaves can form at different locations upstream of the nozzle exit, although they all depend on the pressure ratio. Ideal flow occurs when $P_{amb} = P_{exit}$, assuming that the flow at the exit of the nozzle is parallel to the nozzle wall. In this regime, the flow isentropically expands through the nozzle and minimal shockwaves form in the supersonic wake[41]. This regime is optimal for chemical kinetics experiments as the temperature variation from the mean in the jet is the smallest in this regime. Underexpanded flow occurs if the ambient pressure is lower than the nozzle exit pressure ($P_{amb} < P_{exit}$). The flow undergoes a Prandtl-Meyer expansion at the nozzle exit, which causes a series of repeated oblique and reflected shocks to form downstream past the nozzle exit jet that are impinged by the jet boundary[44,45]. Macroscopic quantities vary over these shockwaves hence the temperature varies sinusoidally across these shockwaves until the jet breaks up. An over-expanded flow is similar to an underexpanded flow although over-expanded flow arises when the ambient pressure is higher than the exit pressure ($P_{amb} > P_{exit}$).

III. METHODOLOGY

A. Experimental

1. Laval Nozzles

The nozzles tested in this study were originally designed using a code developed by Atkinson and Smith[11], which is based on the MOC/BL approach. All of the nozzle profiles used in this study were manufactured from steel using a CNC machine, with a smooth surface finish. The average roughness of the nozzle was not characterised as part of this study although machined steel has an approximate average roughness of less than 3.2 μm[46]. The characteristic dimensions of each of the nozzles, along with the design Mach number and design gas are seen in Table I. Note that in Section V, the same nozzle has been used with different gases. Different gases can be used with the same nozzle and different pressures to generate a variety of temperatures. The tests performed on both apparatuses were conducted with the same machined nozzle as it was moved between groups during testing. The nozzles, together with a schematic showing the key dimensions are shown in Figure 3.

2. Experimental Apparatus and Operation

A brief generalised overview of the experimental method used at the University of Leeds and University of Birmingham is given, with a more detailed description in Taylor et

TABLE I. Main characteristic dimensions of the Laval nozzles used in this study. L_n is the nozzle length, $L_{n-50\%}$ is the half-length, L_{n-thr} is the distance from the nozzle inlet to the throat, d_{n-in} is the inlet diameter, d_{n-thr} is the throat diameter, $d_{n-50\%}$ is the diameter at half-length and d_{n-out} is the outlet diameter. The design Mach number refers to the Mach number specified in the MOC calculations.

-	Nozzle 1	Nozzle 2
Design Mach Number	2.25	4.00
Design Gas	Nitrogen	Nitrogen
L_n (cm)	4.16	8.81
$L_{n-50\%}$ (cm)	2.08	4.41
L_{n-thr} (cm)	0.40	0.40
d_{n-in} (cm)	1.00	1.00
d_{n-thr} (cm)	0.40	0.40
$d_{n-50\%}$ (cm)	1.24	2.51
d_{n-out} (cm)	1.74	3.31

al.,[8] and Lucas et al.,[47] respectively. The Birmingham apparatus alongside a schematic is shown in Figure 1, a picture of the Leeds apparatus can be found in the supplementary material. The apparatus works in the following way: an inert bath gas, nominally nitrogen, helium or argon is mixed with a diluted reagent. The reagent is generally $< 1\%$ to ensure the jet remains mostly unchanged when carrying out kinetic studies as the jet is characterised without reactants. The gas is pressurised in an upstream ballast tank, where the mass flow into the tank is monitored using a set of calibrated mass flow controllers (MKS instruments), and is routed to the pulsed valves using flexible tubing. The gas is pulsed through two solenoid valves (Parker 9 series) with a pulse width of 2-20 ms at a rate of 10 Hz into a high-pressure pre-expansion reservoir region. The reservoir is connected to a Laval nozzle (typically < 5 cm in exit diameter) which is sealed to the reservoir using an o-ring to prevent leakage. The reservoirs used at both Leeds and Birmingham are not temperature controlled, and are approximately at room temperature.

TABLE II. Characteristic dimensions of the CRESU apparatus at both the University of Leeds and University of Birmingham. The reservoir and chamber are taken to be perfect cylinders. The mathematical symbols refers to the dimensions on Figure 6.

-	Symbol	Leeds	Birmingham
Chamber Radius (cm)	r_{chm}	12.0	19.8
Chamber Length (cm)	L_{chm}	77.4	100
Reservoir Radius (cm)	r_{res}	0.50	2.30
Reservoir Length (cm)	L_{res}	1.00	1.83
Reservoir Volume (cm^3)[a]	-	0.79	30.75
Outlet Diameter (cm)[b]	d_{out}	15.0	15.0
Outlet Position (cm)	L_{out}	55.0	87.5
Pulsed Valve Orifice (cm)	d_{in}	0.294	0.294

[a] Reservoir size and volume do not account for auxiliaries, including connected pipes and valves.
[b] Outlet diameter refers to the diameter of the flange the vacuum pump is connected to. The outlet position is the distance from the outlet from the from the leftmost vacuum chamber wall.

The gas expands from the reservoir through the Laval noz-

FIG. 3. Picture of Nozzle 1 (left) and Nozzle 2 (middle) used in experiments and a schematic of an arbitrary nozzle (right) profile with the main characterising dimensions as shown in Table I. Blue coloured section refers to the converging section and green coloured refers to the diverging section. Dimensions for nozzles used in this study can be seen in Table I.

zle into a large vacuum chamber (evacuated using vacuum pumps) forming a low-temperature, axisymmetric, supersonic jet that extends tens of centimetres downstream of the nozzle exit. The flow in this region is collimated and thermalized, allowing molecular reactions to be studied, usually with Pulsed Laser Photolysis Lased Induced Fluorescence (PLP-LIF)[2,8,9]. For the work presented here, no reactants are required for flow characterisation as no reactions are taking place, therefore the gasses used for experiments were nitrogen (99.998%, BOC), helium (99.998%, BOC) and argon (99.998%, BOC).

The main characterising dimensions of the pre-expansion reservoir and vacuum chamber for both the Leeds and Birmingham groups are shown in Table II. The outlet diameter refers to the diameter of the flange that the vacuum pump is connected to, and the outlet position is the distance of this flange from the opposite end of the chamber. The Birmingham apparatus has a much larger reservoir and vacuum chamber, the effects of which will be discussed later in this study.

3. Pitot Tube Characterisation

Both experimental apparatuses used in this study allow incremental control of the Pitot tube location through the use of translatable stages which are electronically controlled using stepper motors. Laser alignment is used to ensure that the Pitot tube is located on the centerline of the nozzle. In the Leeds apparatus, the Pitot tube can move 0 - 30 cm in 0.9 mm intervals with an accuracy of ± 1 mm with respect to the nozzle exit ($x = 0$)[8]. Whilst in the Birmingham apparatus, the Pitot can move from 0 - 60 cm with an accuracy of ± 0.15 mm. The Pitot tube mounting assembly used by both Leeds and Birmingham is a form of an L type bracket, which is bolted to the translation stage, as shown in Figure 4. A picture of both the Pitot tubes used at the Univeristy of Leeds and University of Birmingham is shown in supplementary material.

The Pitot tube used to measure the impact pressure at Leeds is a fast-response absolute pressure transducer (Honeywell 176PCH Series), which has an outer diameter of 7.00 mm. At Birmingham, the Pitot tube used is a differential pressure transducer (Honeywell HSCSAAN001PDAA5) with an outer diameter of 4.93 mm. Both groups monitor the reservoir pressure using a calibrated pressure transducer located on the
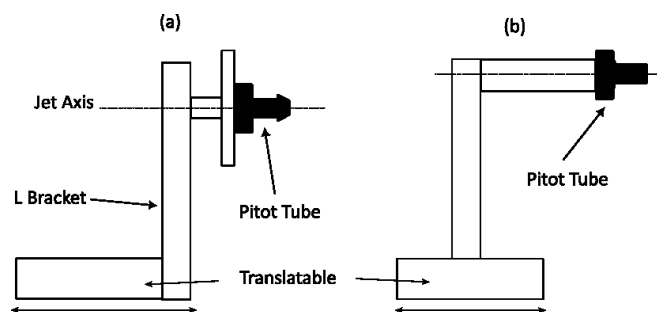

FIG. 4. Side profile of the mounting solution for the Pitot tube used at (a) the University of Birmingham and (b) the University of Leeds. The mounts are connected to translation stages via the bottom bracket. The diagram is not to scale.

reservoir wall, and the vacuum chamber pressure is monitored using calibrated capacitance manometers. The gas pulse duration is always significantly longer than the time over which kinetic measurements are taken. The time for the gas to leave the nozzle exit to the point at which it breaks up is on the order of 100 to 600 μs compared with the pulse width of ≈ 10 ms, therefore the jet reaches a steady state, and pressure measurements for both impact pressure and reservoir pressure are averaged only once steady state operation is achieved at each Pitot tube location. During a single characterisation, the Pitot tube is positioned at the nozzle exit ($x = 0$) and moved downstream in set intervals until either it reaches its maximum or a user-specified distance from the nozzle exit. At each Pitot tube location, the impact pressure, chamber pressure and reservoir pressures are recorded and can then be used with Equations 3 - 6 to characterise temperature, density, Mach number and pressure of the flow across the jet centerline. An example of an experimental temperature profile is shown in Figure 5.

The performance of a particular jet is generally characterised by the average temperature T_{avg} across the stable flow region (L_{flow}) and the error for kinetic measurements is taken to be one standard deviation around the mean ($\pm\sigma_T$) also in the stable flow region. It is common practice in the chemical kinetics community to quantify the jet performance by $T_{avg} \pm \sigma_T$. Alongside temperature, the Mach number, density and pressure are given in the same format (i.e. $M_{avg} \pm$
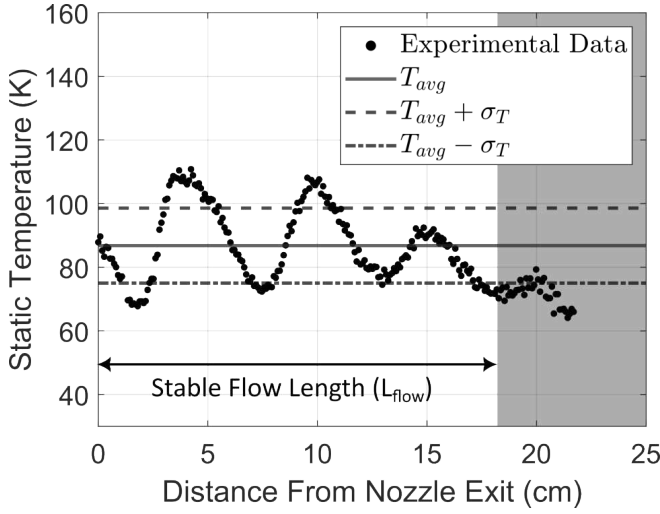
FIG. 5. Typical static temperature profile obtained from impact pressure measurements taken across the centerline of an arbitrary supersonic jet, Temperature is obtained by using the impact pressure with the Rayleigh-Pitot equation and adiabatic relationships which are given in Equation 1 and Equations 4 - 6 respectively.

σ_M) across the stable flow length to provide more information about the jet.

The point at which the flow breaks down is typically interpreted during the post-processing of experimental data. This can be seen clearly as the structure of the jet breaks down, and the temperature decreases one standard deviation below the mean. The reason why the apparent temperature decreases where the jet breaks down is explored in section III C.

For a given nozzle, the optimal jet is obtained by varying either or both the reservoir and chamber pressure, which alters the P_{exit} and P_{amb} of the system. At each value of chamber and reservoir pressure, a characterisation profile is recorded and the profiles are compared. The one with the smallest σ_T, assuming the flow length is longer than ≈ 15 cm is considered optimal as it has the lowest error from the mean temperature. This is considered optimal as this allows rate coefficients to be more precise.

B. Numerical Methods

1. Governing Equations

The flow is characterised by low density, low viscosity and high Mach number. In all the cases, the Reynolds number (Re) > 1000 and M < 5. The Knudsen Number (Kn) is dependent on the Reynolds number and Mach number and can be calculated using $Kn = \frac{M}{Re}\sqrt{\frac{\gamma\pi}{2}}$[48]. Therefore as $Kn << 0.01$, the flow can be modelled as a continuum. To model high-speed compressible flow, dependent macroscopic quantities are density-weighted and filtered using Favre-averaging[49]. The Favre-averaged mass, momentum and energy continuity

equations assuming the fluid is Newtonian and isotropic are:

$$\frac{\partial\bar{\rho}}{\partial t} + \frac{\partial}{\partial x_j}(\bar{\rho}\tilde{u}_j) = 0 \tag{8}$$

$$\frac{\partial(\bar{\rho}\tilde{u}_i)}{\partial t} + \frac{\partial}{\partial x_j}(\tilde{u}_i\bar{\rho}\tilde{u}_j) = \frac{\partial\bar{P}}{\partial x_i} + \frac{\partial\bar{\sigma}_{ij}}{\partial x_j} + \frac{\partial\tau_{ij}}{\partial x_j} \tag{9}$$

$$\frac{\partial(\bar{\rho}\tilde{E})}{\partial t} + \frac{\partial}{\partial x_j}(\tilde{u}_j\bar{\rho}\tilde{H}) = \frac{\partial}{\partial x_j}\left(\bar{\sigma}_{ij}\tilde{u}_i + \left(\mu + \frac{\tilde{\mu}_t}{\sigma_k}\frac{\partial k}{\partial x_j}\right)\right)$$
$$- \frac{\partial}{\partial x_j}\left(\frac{c_p\tilde{\mu}_t}{Pr}\frac{\partial\tilde{T}}{\partial x_j} + \frac{c_p\tilde{\mu}_t}{Pr_t}\frac{\partial\tilde{T}}{\partial x_j} + \tilde{u}_i\tau_{ij}\right) \tag{10}$$

where ρ is the fluid density, u_i is the fluid velocity component, P is the fluid pressure, T is temperature, $\bar{\sigma}_{ij}$ is the mean viscous stress, τ_{ij} is the Reynolds stress tensor, μ_t is the turbulent viscosity and k is the turbulent kinetic energy. Variables indicted with overbar ($\bar{\rho}_i$) and tilde ($\tilde{u}_i$, $\tilde{u}_k$) represent the Reynolds averaged and Favre-averaged quantities respectively. $\tilde{E}$ is mean energy, $\tilde{H}$ is the mean fluid enthalpy. The Prandtl number is defined as $Pr = c_p\mu/\kappa$, where κ is thermal conductivity, and c_p is the specific heat capacity of the fluid. The turbulent Prandtl number Pr_t is set to 0.9. The ideal gas law ($P = \rho RT$) was used as an equation of state, where R is the ideal gas constant. The temperature dependence on viscosity (μ), specific heat capacity (c_p) and thermal conductivity (κ) for each gas used (nitrogen, argon and helium) was modelled by fitting polynomials to fluid properties obtained through the NIST database. Pressure dependency on μ, c_p and κ was assumed to be negligible. The Reynolds stress tensor is closed using the Boussinesq approximation:

$$\tau_{ij} = 2\tilde{\mu}_t\left(\tilde{S}_{ij} - \frac{1}{3}\frac{\delta\tilde{u}_k}{\partial x_k}\delta_{ij}\right) = \frac{2}{3}\bar{\rho}k\delta_{ij} \tag{11}$$

where δ_{ij} is the Kronecker delta and the turbulent viscosity is unknown as needs and will be discussed in Section III B 2.

2. Turbulence Modelling

The k-ω shear stress transport (SST) was used with viscous heating and no turbulent compressibility effects. This is a two-equation eddy viscosity turbulence model that is used to close the Reynolds stress tensor and was developed by Menter in 1993[50–52], It is a zonal model which blends the Wilcox k-ω model[52], which is used in the near wall region, as it is superior in determining boundary layer formation and flow separation, and uses k-ε by Launder & Spalding[53] in the far-field, which reduces solution dependence on freestream values. It has been shown by various authors that is can accurately resolve large flow gradients (shockwaves) and predict flow separation in supersonic flows[29,42,54]. The eddy viscosity hypothesis proposed by Prandtl[55] is widely used to relate the turbulent

viscosity to the turbulent length scale and the Kolmogorov energy cascade, it is defined as:

$$\mu_t = \bar{\rho}\frac{k}{\omega} \qquad (12)$$

The turbulent transport equations for turbulent kinetic energy (k) and turbulent dissipation (ω) are as follows (note these are scalar quantities):

$$\rho\frac{\partial k}{\partial t} + \rho\tilde{u}_j\frac{\partial k}{\partial x_j} = \tau_{ij}\frac{\partial\tilde{u}_i}{\partial x_j} - \beta^*\rho\omega k$$
$$+\frac{\partial}{\partial x_j}\left[(\mu + \sigma_k\frac{\bar{\rho}k}{\omega})\frac{\partial k}{\partial x_j}\right] \qquad (13)$$

$$\rho\frac{\partial\omega}{\partial t} + \bar{\rho}\tilde{u}_j\frac{\partial\omega}{\partial x_j} = \frac{\gamma}{v_t}\tau_{ij}\frac{\partial\tilde{u}_i}{\partial x_j}$$
$$-\beta\bar{\rho}\omega^2 + \frac{\partial}{\partial x_j}\left[(\mu + \mu_T\omega_\sigma)\frac{\partial\omega}{\partial x_j}\right]$$
$$+2\bar{\rho}(1-F_1)\sigma_{\omega,2}\frac{1}{\omega}\frac{\partial k}{\partial x_j}\frac{\partial\omega}{\partial x_j} \qquad (14)$$

where β, β^*, σ_k, σ_ω and γ are turbulence closure coefficients, and v_T is the kinematic eddy viscosity. F_1 is a function used to blend between the respective models and is dependent on flow location with respect to the nearest wall. This blending can be achieved using[50]:

$$F_1 = tanh(arg_1^4) \qquad (15)$$

$$arg_1 = min(max(\frac{\sqrt{k}}{0.09\omega y}; \frac{500v}{y^2\omega}); \frac{4\rho\sigma_{\omega,2}}{kCD_{k\omega}y^2}) \qquad (16)$$

$$CD_{k\omega} = max(2\rho\sigma_{\omega,2}\frac{1}{\omega}\frac{\partial k}{\partial x_j}\frac{\partial\omega}{\partial x_j}, 10^{-20}) \qquad (17)$$

where y is the distance from the nearest wall and CD_{kw} relates to the cross-diffusion term on the RHS of Equation 14. As the SST model is a zonal model, the closure coefficient is also blended with respect to flow location. This is achieved using:

$$\phi = F_1\phi_1 + (1-F_1)\phi_2 \qquad (18)$$

where ϕ corresponds to the SST closure coefficient, while ϕ_1 and ϕ_2 relate to the closure coefficients in the k-ω and standard k-ε models respectively. The stress is limited by modifying the kinematic eddy viscosity using a similar blending function:

$$F_2 = tanh(arg_2^2) \qquad (19)$$

$$arg_2 = max(2\frac{\sqrt{k}}{0.09\omega y}; \frac{500v}{y^2\omega}) \qquad (20)$$

$$v_t = \frac{a_1 k}{max(a_1\omega; \Omega F_2)} \qquad (21)$$

where a_1 is a constant and Ω is the shear strain rate. The closure coefficients used for all cases can be seen below:

k-ω: (ϕ_1): $\sigma_{k,1} = 0.85$, $\sigma_{\omega,1} = 0.5$, $\beta_1 = 0.075$, $\beta^* = 0.09$, $\gamma_1 = \frac{\beta_1}{\beta^*} - \frac{\sigma_{\omega,1}\kappa^2}{\sqrt{\beta^*}}$, $\kappa = 0.41$, $a_1 = 0.31$

k-ε: (ϕ_2): $\sigma_{k,2} = 1.0$, $\sigma_{\omega,2} = 0.856$, $\beta_2 = 0.0828$, $\beta^* = 0.09$, $\gamma_2 = \frac{\beta_2}{\beta^*} - \frac{\sigma_{\omega,2}\kappa^2}{\sqrt{\beta^*}}$, $\kappa = 0.41$, $a_1 = 0.31$

3. Computational Domain & Boundary Conditions

To capture the differences between the two experimental apparatus at Leeds and Birmingham, the numerical simulations are carried out with a variety of different dimensions for the reservoir, nozzle and vacuum chamber. Therefore Figure 6 is a generalisation of the geometry setup, and the respective dimensions for each apparatus are given in Table II. The reservoir, chamber and nozzle dimensions used in subsequent studies will be denoted by the reactor setup used, i.e. Leeds (L) or Birmingham (B) and the nozzle geometry i.e. Nozzle 1 or Nozzle 2. The pressures set in the CFD for Nozzle 1 are averaged from the experiments, and are given in Table III. These pressures have been experimentally optimised by both groups to give the best-performing jet, which is the one with the lowest standard deviation of temperature.

The nozzle geometry was constructed using a spline, estimated using a series of evenly spaced points generated originally determined using the MOC/BL program. The outlet diameter (d_{out}) was area-scaled to account for the annulus that forms when the outlet is resolved axisymmetrically. The inlet diameter (d_{in}) was kept to be the diameter of the valve orifice, as scaling caused issues with numerical divergence. To ensure the results were not dependent on the inlet opening, a study was performed as shown in Section III C 1 reducing the inlet diameter, which showed a negligible change in flow structure and mass flow rate through the system. The inlet and outlet pressure boundaries are set to a Dirichlet pressure inlet (P_{res}) and pressure outlet (P_{chm}) respectively, both acting normally to the boundary. The pressures set at these boundaries for Nozzle 1 have been averaged from the experimental pressure transducers from both the Leeds and Birmingham apparatus is shown in Table III. The inlet pressure relates to the reservoir pressure, and the outlet pressure relates to the vacuum chamber pressure used in the experiments. The inlet and outlet temperature were set to 300 K and 293 K for the Leeds and Birmingham cases respectively. The temperature boundary conditions are set according to previously reported conditions for Leeds[8] and Birmingham[47]

TABLE III. Reservoir and chamber conditions used in experiments by Leeds and Birmingham to obtain optimal flow conditions. P_{res} and P_{chm} refers to the reservoir and chamber pressure respectively. Turbulent intensity (I) has been estimated as it is unknown, although the effects of this are discussed in Section III C. The chamber and reservoir pressures used are averaged from one experiment for each group.

-	Nozzle 1 - L	Nozzle 1 - B
Reservoir Pressure (P_{res})	5222.7 Pa	5203.5 Pa
Chamber Pressure (P_{chm})	170.7 Pa	169.7 Pa
Turbulent Intensity (I)	1.0%	1.0%

In the absence of absolute measurement, turbulent intensity (I) on the inlet and outlet boundary was set at 1%, with a sensitivity study on inlet turbulent intensity carried out in Section IV (outlet turbulent intensity has a negligible impact on results). The jet is typically 10-15 diameters away from

the chamber wall, and the nozzle and reservoir block acts as a large heat sink so adiabatic conditions alongside no-slip conditions are applied to all wall surfaces.

The bottom edge was set to an axisymmetric symmetry boundary as the supersonic jet is rotationally invariant. The main limitation of the axisymmetric approach is that the outlet in the experiments is asymmetric as it is located on one side of the vacuum chamber and that there are only two inlet pipes to the reservoir. The asymmetry of the outlet is assumed to have a negligible impact on flow structure as the jet is supersonic. This was tested and confirmed by comparing the 2D axisymmetric and 3D cases, more information can be seen in supplementary material.

The 2D axisymmetric model was adopted as this model has been shown to achieve near identical results to the 3D case in this study and by various authors working on similar studies and is computationally inexpensive in comparison[29,31,33,38]. The 2D axisymmetric method allows substantially faster nozzle prototyping capabilities and will be used herein.

Transient simulations using the 2D axisymmetric setup have not been included in this study. Experimental groups using the pulsed CRESU apparatus have repeatedly shown that the pressure measurements (impact, chamber and reservoir pressures), and in turn the supersonic jet reaches a steady state before kinetics measurements are made[8,12,16,40]. The duration of a gas pulse is $\approx$ 10 ms, and the time in which kinetic measurements are made is on the order of $\approx$ 500 μs (although depends on jet length and reaction).

To obtain the approximate length of the stable flow region in all of the numerical results presented, a two step procedure was adopted. As the axial density profile is sinusoidal like the temperature profile, the last peak (furthest from the nozzle exit) can be used to approximate where the flow breaks down. First the locations of the local maxima of axial density profile is calculated. The approximate stable flow length is then taken to be the furthest local maxima away from the nozzle exit. The quantities such as average temperature, Mach number are calculated from the nozzle exit (x = 0) up to the stable flow length (L_{flow}).

4. Numerical Simulations

The double precision implicit pressure-based finite volume solver within Ansys Fluent 2022R1 was used with second-order discretization schemes for spatial gradients. Density-based solvers are typically employed for supersonic flows, although studies were performed comparing the solver performance, and the pressure based showed faster convergence performance with near identical results at $M = 3$, and similar results at $M > 3$, similarly found by Besagni & Inzoli[32], these results are shown in the supplementary material. Steady-state calculations were initialised using the full multi-grid (FMG) technique and were run until convergence criteria of 1×10^{-5} ($\approx$ 500-700 iterations) was obtained for all residuals. Automatic mesh adaption was carried out every 250 iterations to ensure the $y^+ < 1$ on all walls to ensure flow separation was captured. A Pseudo-transient approach was used, with a time

factor of 0.5 to improve convergence. Numerical work was undertaken on ARC4, part of the High-Performance Computing (HPC) facilities at the University of Leeds, UK. The HPC facilities at the University of Birmingham, UK, were also utilised for testing and validation of the CFD framework discussed in Section V.

5. Meshing Strategy and Mesh Independence

Structured quadrilateral elements were used to reduce computational costs, improve solution accuracy, and reduce numerical diffusion. The elements were aligned with the flow direction and clustered towards walls to resolve the boundary layer, ensuring the $y^+ < 1$ as seen in Figure 7. Elements were also clustered towards the left chamber wall as the largest magnitude shock and largest flow gradients occurred in this region.

The comparison of static axial temperature across the axis of the flow for meshes of increasing density using Nozzle 1 with the Leeds setup and conditions is shown in Figure 8.

A grid convergence study using Richardson extrapolation[56] was conducted, again using Nozzle 1 with the Leeds apparatus and conditions, the results are shown in Table IV. The grid convergence index (CGI) was calculated using:

$$CGI(\%) = \frac{F_s|\varepsilon|}{(z^p - 1)} \ where, \ \varepsilon = \frac{f_2 - f_1}{f_1} \qquad (22)$$

and p using a constant grid refinement ratio can be found by:

$$p = ln\left(\frac{f_3 - f_2}{f_2 - f_1}\right)/ln(z), \qquad (23)$$

where F_s is a safety factor, taken to be 1.25, z is the refinement ratio, taken as 2 and f_1 relates to the finest grid. The number of elements required to resolve the main features of interest without excessive computation was 537,170, resulting in 10 cells per mm in the nozzle exit region. The discretization error (CGI) for the average temperature across the stable flow length for runs 1-3 and 2-4 was found to be 0.100% and 0.007% respectively, with the results shown in Table IV. A mesh independence study was also carried out using Nozzle 2 using a similar mesh, which is a longer Mach 4 nozzle, where results can be found in supplementary material.

TABLE IV. Mesh Independence results from Nozzle 1 using nitrogen and pressure conditions given in Table III. The values are average Mach (M_{avg}) and average static temperature (T_{avg}) plus or minus one standard deviation and are taken across the axis of the stable region of the jet past the nozzle exit. GCI refers to the grid convergence index.

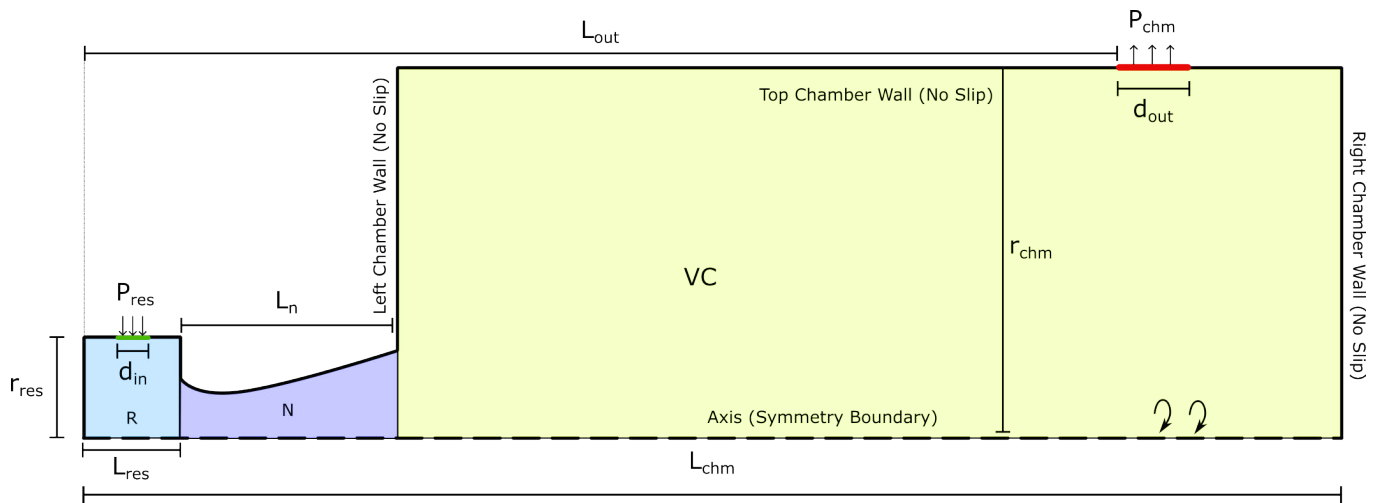| Elements	$M_{Avg} \pm \sigma_M$	$T_{avg} \pm \sigma_T$ (K)	CGI (%)
32,534	2.885 $\pm$ 0.200	113.52 $\pm$ 10.20	-
133,294	2.910 $\pm$ 0.217	112.01 $\pm$ 10.30	-
539,255	2.916 $\pm$ 0.226	111.65 $\pm$ 10.53	0.100
2,164,249	2.917 $\pm$ 0.230	111.60 $\pm$ 10.60	0.007

FIG. 6. Schematic of the geometry used in the freestream CFD cases, the pressure inlet (P_{res}) is denoted by a green line, the pressure outlet (P_{chm}) by a red line, and all no-slip walls are denoted by thick black lines. The sections denoted R, N and VC and the reservoir, nozzle and vacuum chamber respectively. Labelled dimensions relate to Table II in the experimental section. The nozzle and reservoir are placed so that it is in the leftmost position within the chamber.
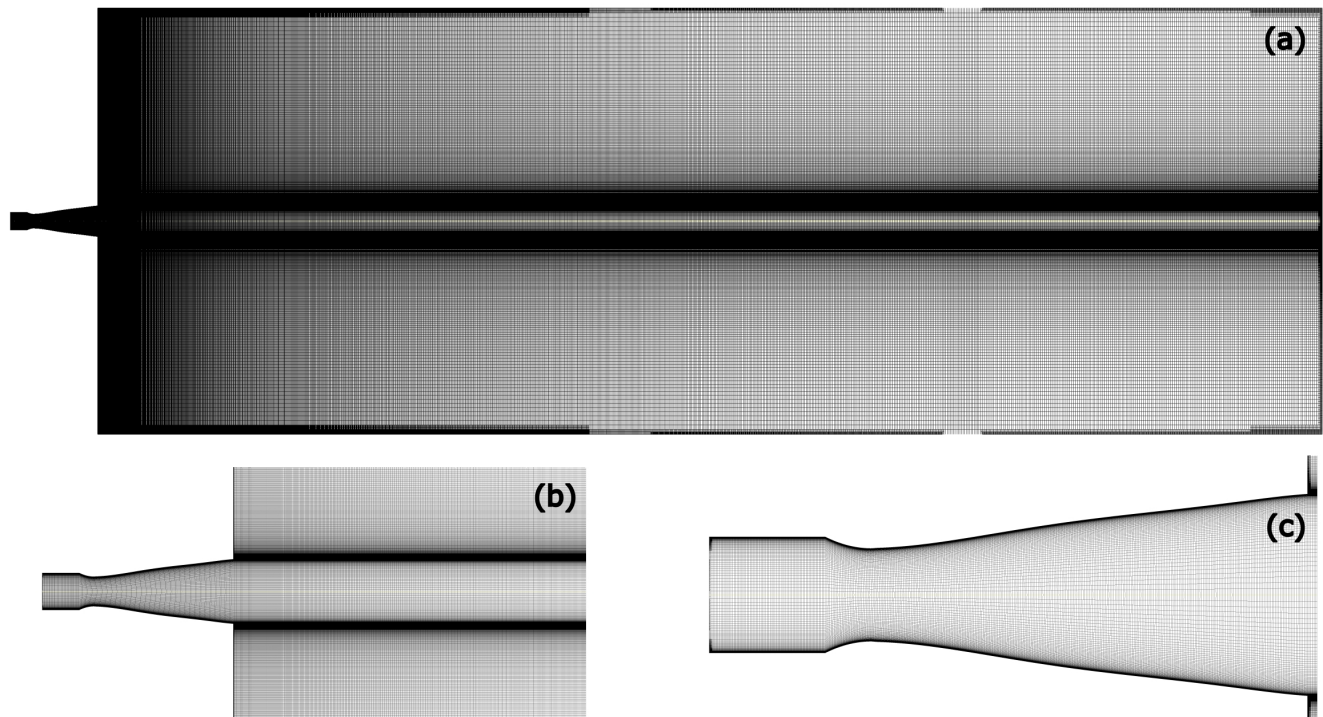

FIG. 7. Mesh used for the M2.25 Nozzle with the Leeds reservoir and chamber dimensions. An overall view of the mesh structure is shown in (a), with a closeup of the nozzle seen in (b) and (c). The mesh has been mirrored across the axis and the number of elements in this domain is 537,170.

C. Sensitivity Studies

1. Solver Settings and Boundary Conditions

A variety of studies were conducted to ensure a robust computational framework, these included varying inlet tempera-ture, outlet position, inlet size, discretisation scheme, solver type, convergence criterion and surface roughness. These are shown to provide insight into how insensitive the numerical model is when changing parameters and to give guidelines to what solver settings are required to resolve the important flow structures of the jet. The axial static temperature profiles from the sensitivity studies that are shown in Figure 9 use Nozzle 1
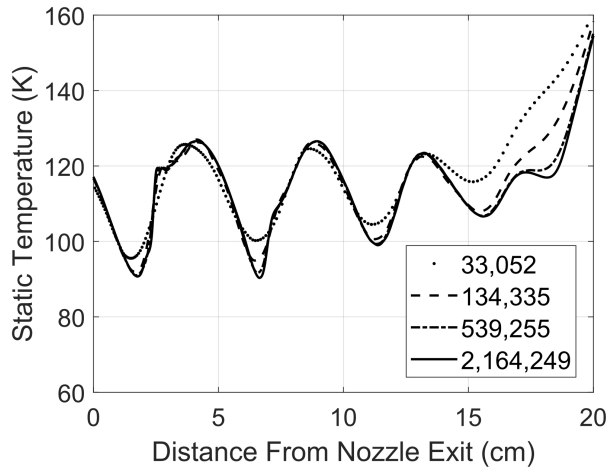
FIG. 8. Effect of increasing the number of mesh elements on the 1D axial static temperature for Nozzle 1 using parameters of the Leeds apparatus.

with the Leeds conditions given in Table III and with the mesh containing 539,255 elements.

Figure 9a shows the effect of changing the temperature on the inlet boundary, which refers to the temperature of the gas entering the reservoir. Decreasing the inlet temperature has no impact on the structure or Mach number of the jet, this is apparent as the profiles align when the temperatures are shifted. A 10 K drop to 290 K causes a ≈ 4 K reduction in average temperature, while a further drop by 10 K to 280 K results in a further ≈ 3 K drop in temperature. The average jet temperature can be decreased by lowering the inlet temperature, although this comes with diminishing returns the lower the temperature of the inlet gas. This shows that the same nozzle can be used to achieve a large range of temperatures if the inlet gas is heated or cooled. Cooling of the reservoir has already been exploited experimentally to achieve the lowest recorded temperature of 5.8 K in 2010[17].

Moving the outlet position further away from the nozzle exit increases the flow length by < 1%, as shown in Figure 9b. To ensure the flow length is as long as possible for reaction kinetics, it is recommended that the outlet should be placed as far as possible from the nozzle exit. If the inlet is closer to the nozzle exit, the gas hits the opposite end of the vacuum chamber wall and circulates around and above the supersonic wake towards the outlet. This alters the pressure P_{amb} in the chamber. Although the flow can be improved by changing the reservoir or chamber pressure.

As the machined nozzle is not completely smooth (average roughness assumed to be < 3.2 μm), uniform surface roughness was included on the nozzle walls in the CFD to view its effects and is shown in Figure 9c. Increasing the surface roughness height (K_s) reduces the stable flow region as it causes the turbulent mixing layer that surrounds the core to develop earlier compared with a smooth nozzle surface. As the surface roughness is very low with machined steel nozzles, it is not an issue in the current study, although including

roughness effects may be required if nozzles are manufactured using additive manufacturing techniques. It also may be worth noting that machining tolerances were assumed to be 0 in all nozzle profiles but this will not be the case and needs to be looked at in greater detail as variation could be large in comparison to the nozzle dimensions.

The results from increasing the residual tolerances and order of gradient discretisation schemes is shown in Figure 9d and 9e respectively. The residual tolerance required to obtain a smooth solution is 1×10^{-5} and has been used for all cases herein. First-order gradient schemes struggle to capture the shock front and magnitude compared to more accurate second and third-order schemes. Increasing from second-order to more expensive, unstable third-order schemes shows no benefit, therefore only second-order schemes are required to obtain a good flow solution.

The final study that is shown in Figure 9f is the effect of the inlet diameter. Decreasing the inlet diameter from 2.94 mm to 1.00 mm causes a shortening of the flow length by 2.4%, this is because the mass flow rate through the reservoir and nozzle decreases. This suggests that the flow length can be improved by increasing the diameter of the inlet with negligible change to the average temperature and standard deviation. Although this will require a higher mass flow rate through the system. As decreasing the inlet diameter had a minimal effect on the results, and scaling the inlet diameter caused divergence issues, the inlet diameter was left to be the same diameter as the inlet valve diameter.

A mass flow inlet was also investigated numerically using the experimental mass flow of 0.0005 kg/s. This was calculated by taking the standard volumetric flow rate into the ballast tank and multiplying it by 10 as the pulsed valves were operated at 10 Hz with a pulse width of 10 ms. This was converted to mass flow using the density of nitrogen at standard conditions. Using a mass flow inlet boundary resulted in an average nozzle exit pressure of 165.28 Pa and an ambient pressure of 167.84 Pa, therefore as $P_{amb} > P_{exit}$, the flow is overexpanded, and the reservoir pressure is ≈ 500 Pa lower than measured experimentally. This may be because the mass flow inlet is further upstream than the reservoir, and the flow is pulsed so it is hard to obtain an accurate flow rate, therefore a pressure inlet was used for the remainder of the study

2. Inlet Turbulence

The turbulent inlet conditions are unknown and cannot be obtained via experiments due to spatial and equipment limitations. A study was conducted increasing the turbulent intensity from 1-40% using the 2D Axisymmetric RANS model to understand the sensitivity of the turbulent intensity of the inlet boundary on the 1D static temperature profile, as shown in Figure 9g. Increasing the turbulent intensity causes a small reduction in shock magnitude past the first trough, it also increases the rate at which the turbulent boundary layer develops downstream, this is evident as the stable flow length (isentropic core) decreases when increasing turbulence intensity. Increasing the turbulent intensity from 1-10% reduces
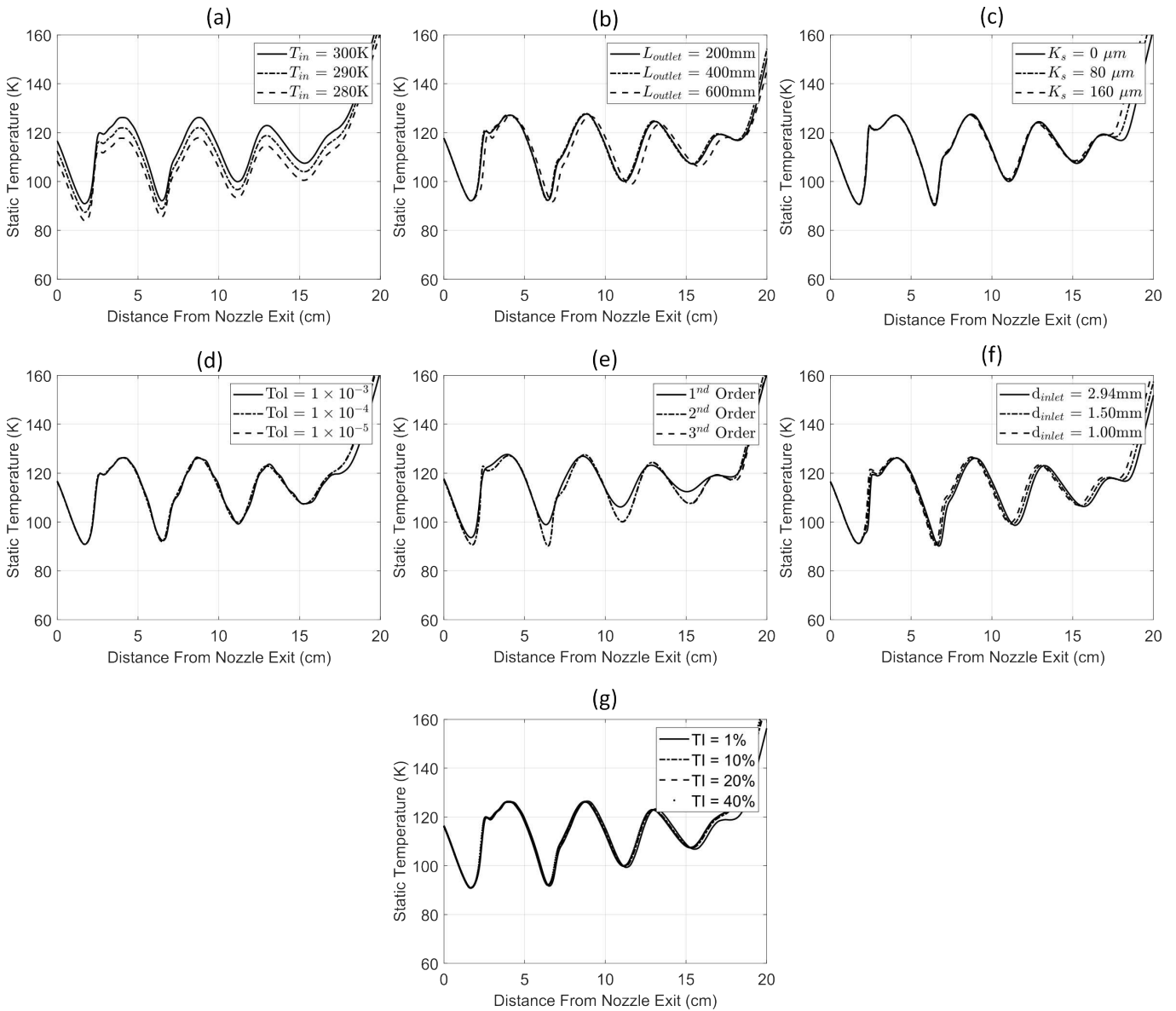
FIG. 9. Results from sensitivity studies showing static temperature across the axis of the jet. Where (a) variation of inlet temperature (b) variation of outlet position (c) variation of uniform surface roughness height (d) variation of residual tolerance (e) effects of spatial gradient order (f) effect of inlet diameter size and (g) effect of inlet turbulent intensity.

the flow length from 18.00 cm to 17.44 cm which is a decrease of 3.1%. The average temperature and standard deviation increases by < 0.1 % for both parameters respectively. Increasing past $I = 10\%$, shows a negligible change in the point-wise solution and global quantities, which is expected as the SST model was developed to be insensitive to turbulent boundary conditions.

There is minimal difference in global flow quantities when increasing the inlet turbulence, therefore the exact value for inlet turbulence is not required as it makes a minimal impact on the global quantities of interest, such as stable flow length, average temperature and the standard deviation of temperature in the stable flow region. Following this, all studies from this point have been calculated using a turbulent

intensity on the inlet boundary as $I = 1\%$.

3. Numerically Characterising the Pitot Tube Effect

A numerical study was conducted to understand the Pitot tube effect in the Leeds setup with 7 mm Pitot tube that is used. The same nozzle, boundary conditions and chamber geometry were used as the freestream benchmark case, although the approximate geometry of the Pitot tube was cut out of the axisymmetric boundary as a blockage to imitate the presence of a Pitot tube in the flow. The Pitot tube was moved across the flow axis in 2 mm intervals from 0.2 cm to 25 cm, to-
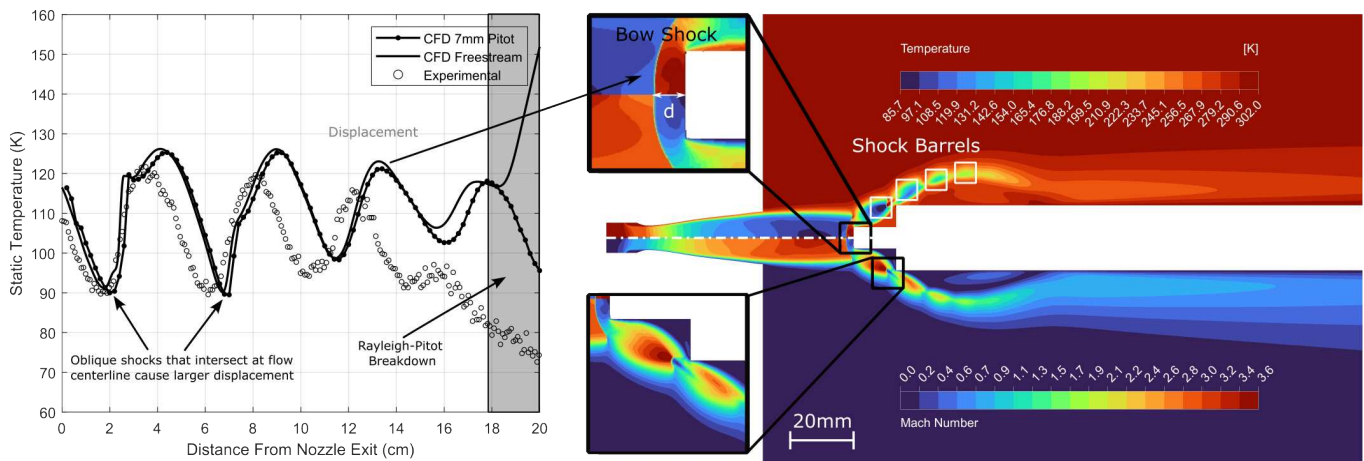
FIG. 10. Results from the numerical Pitot tube study, (left) shows the 1D static temperature profile across the axis of the flow, it also shows the, region of the Rayleigh-Pitot equation breakdown (grey) and displacement between the freestream and Pitot tube cases. (right) show the static temperature contour and Mach number contour, which are separated by the white dotted line. These results are for when the Pitot tube is 50 mm from the nozzle exit. The temperature profile from the Pitot tube CFD case was obtained by taking the impact pressure at the Pitot leading edge and using the Rayleigh-Pitot equation and adiabatic equation to convert it to temperature. Each one of the markers for the Pitot tube data relates to a unique CFD case.

talling 140 simulations, similar to what is carried out experimentally. The mesh density remained unchanged throughout although the number of elements increases as the Pitot tube moves downstream from the nozzle exit (ranges from 150,000 - 1,300,000 elements). As the case is highly non-linear with intersecting shocks, the case was run in first order until converged, and then ran in second order with a pseudo-time factor of 0.05 and reduced under relaxation factors to improve solution stability. At each distance from the nozzle exit, the maximum impact pressure was recorded at the Pitot tube leading edge once the simulation had converged (15000 iterations). This impact pressure was then converted into Mach number using the Rayleigh-Pitot expression from Equation 1 using a reservoir pressure of 5222 Pa. The temperature of the flow at each Pitot location is then calculated using Equation 4 with a reservoir temperature of 300 K. Information on the geometry, meshing setup and mesh independence can be found in supplementary material.

The displacement effect is due to the bow shock that forms on the leading edge of the Pitot tube as shown in Figure 10. The displacement was approximated by locating the distance between the bow shock front and the leading edge of the Pitot tube. The displacement profile across the axis of the jet can be seen in Figure 11. The inclusion of the Pitot tube causes a shift forward in the axial temperature profile by 2-3 mm and the magnitude of the displacement increases downstream of the nozzle exit, similarly found by various authors[26,28]. In this particular case, the displacement increases by 0.02 mm every 1cm downstream of the nozzle exit. The displacement profile is oscillatory, although inversely proportional to the temperature profile i.e. lower temperature, higher displacement. The displacement is related to the flow speed, where a higher flow speed results in a larger displacement from the Pitot tube leading edge. The increased flow speed results in a higher vorticity in the region in front of the bow shock, which pushes

the bow shock backwards, causing increased displacement[27]. There are two locations in the flow where the displacement is much larger than the underlying oscillatory displacement profile. These occur at 2.2 cm and 7.0 cm. These locations relates to where the oblique shocks converge and get reflected at the jet centerline, as shown in Figure 13. The interactions of these oblique shockwaves and its interaction with the bow shock that forms on the Pitot tube could be cause of this, although further investigation is needed. Shockwaves are irreversible discontinuities in the flow, meaning they are a source of entropy. The Rayleigh-Pitot equation assumes that the flow is isentropic, although as the error between freestream CFD and Pitot tube CFD cases is small, the Rayleigh-Pitot equation can be used to characterise a supersonic wake containing weak shockwaves.

The average temperature and Mach number along with the standard deviation of these parameters across the stable jet axis for the Pitot tube case is 110.06 ± 10.18 K and 2.95 ± 0.22 respectively. Comparing these results to the freestream RANS case results in a 1.4% and 1.0% difference in average temperature and Mach number respectively.

The deviation of the results from the freestream CFD case compared to when using the Pitot tube increases downstream at $x = 17$ cm, this may be attributed to the reduction of the isentropic core in this region, meaning the flow is starting to become turbulent in this region, causing the Rayleigh-Pitot equations to under predict the temperature of the last trough by ≈5 K. The flow breakdown for the freestream and Pitot cases break down at the same location at 18 cm from the nozzle exit. It can also be seen in Figure 10 that once the flow has broken down, the temperature decreases, similarly seen in the experimental results. This is because the Rayleigh Pitot equation breaks down as it is no longer in the isentropic core region of the flow. As the Pitot tube does not make a large difference to the global flow quantities, the freestream results are good
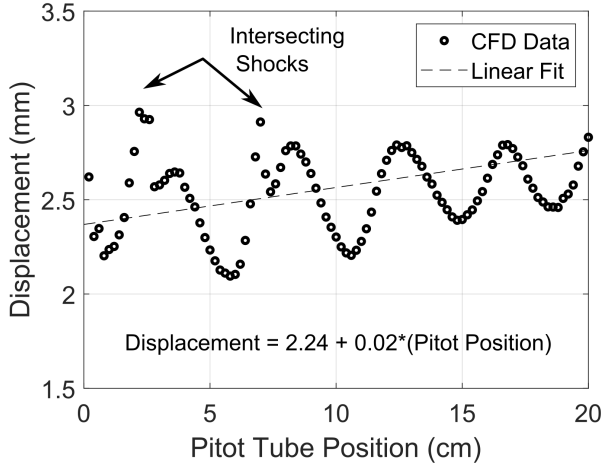
FIG. 11. Pitot tube displacement profile obtained from the CFD using Nozzle 1 and Leeds setup, with the 7 mm Pitot tube, each point is a separate CFD simulation. The displacement is the distance from the leading edge of the Pitot tube to the bow shock. The intersecting shocks relate to the position at which the oblique shocks meet at the centerline.

enough in predicting flow quantities. The freestream case also takes is significantly cheaper in terms of computational time. Using 40 cores. the freestream case without a blockage took 8 minutes to compute, whereas the more complex Pitot tube study containing 140 individual cases took $\approx$ 6 days on 40 cores.

As the blockage effect of the Pitot tube has been shown to decrease when reducing the Pitot tube diameter (i.e. the Pitot tube used at Birmingham) in the literature[26], only one study was performed with the 7 mm Pitot tube at Leeds. It is expected that the smaller Pitot tube used in the Birmingham apparatus will output impact pressure results much closer to the freestream values, although this could be investigated further as the mounting solution differs between the two groups.

From the sensitivity studies performed, it can be concluded that the proposed freestream axisymmetric 2D computational model is robust and highly insensitive to the Pitot tube blockage, vacuum outlet location, and the diameter of the pressure inlet into the reservoir block. Therefore the 2D axisymmetric model will be used throughout the remainder of the study.

IV. RESULTS & DISCUSSION

A. Test Case: Nozzle 1

1. Numerical and Experimental Comparison

All results in this section were carried out using Nozzle 1 with the conditions shown in Table III, which is used with the respective groups' reservoir and chamber geometry given in Table II. If a different reservoir and chamber setup is used, it will be detailed in the respective figures.

Figure 12 shows the 1D temperature profile across the axis of the jet past the nozzle exit for Nozzle 1 using the Leeds apparatus. The static temperature is oscillatory across the jet axis and this structure is a result of the repeating oblique shocks, reflected shocks and expansion fans that form downstream of the nozzle exit. The sharp temperature changes are caused by irreversible flow discontinuities that occur over these shockwaves. The shockwave structure was formed using numerical schlieren and is shown in Figure 13d. Oblique shocks propagate from the nozzle exit to the jet axis at an angle of approximately $20°$, which is very close the analytical angle of $20.5°$ (using M = 2.85, averaged from nozzle exit excluding BL). This shock is then reflected to the jet boundary from the jet axis. When the shock is reflected off the boundary layer, it generates expansion fans which cause the flow to expand and lower in temperature. The discontinuities that occur over these shocks is shown in Figure 13, where sharp temperature gradients occur between the shocks.

The experimental results in Figure 12 show a decline in temperature post breakdown, whereas the CFD increases, this is a limitation of the Rayleigh-Pitot method and adiabatic relationships used to calculate the Mach number, temperature and pressure. The limitations of these equations are discussed previously in Section III C 3. There are 4 main shock barrels that form and the length of these features can be distinguished by the trough-to-trough distance seen in Figure 12. The shock barrel length decreases across the axis, where the average shock barrel length for the CFD and experimental results are 4.63 cm and 4.32 cm respectively. The stable flow lengths for both the experimental and CFD results are 15.9 cm and 18.0 cm respectively. Surrounding the shock barrels, a turbulent mixing layer forms due to viscous shearing and develops downstream. This acts to dissipate the energy within the isentropic core, leading to a reduction in the core diameter as shown in Figure 13.

TABLE V. Comparison of experimental and numerical values for major axial flow quantities across the stable flow region. The value given is the average value $\pm$ one standard deviation. T is the static temperature, M is the Mach number, L_{flow} is the length of the stable region.

-	Experimental	CFD	Difference
$T_{avg} \pm \sigma_T$ (K)	104.5 ± 9.5	111.6 ± 10.6	7.1 ± 1.1
$M_{avg} + \sigma_M$	3.07 ± 0.236	2.92 ± 0.2	0.15 ± 0.01
L_{flow} (cm)	15.9	18	2.1

The CFD is excellent at predicting the location and magnitude of the first shock, and the results become increasingly out of phase downstream of the nozzle exit, this is commonly seen throughout the literature when using the k-ω-SST turbulence model, and can struggle to predict shockwave boundary layer interactions and mixing layer development across the jet. This may be amplified due to the large pressure ratios used (> 30) that are being used in this study. Mubarak & Tide[33] compared numerical results and experimental PIV results of Laval nozzles at low pressure ratios (< 5), which showed the same exact shifting behaviour which increases downstream
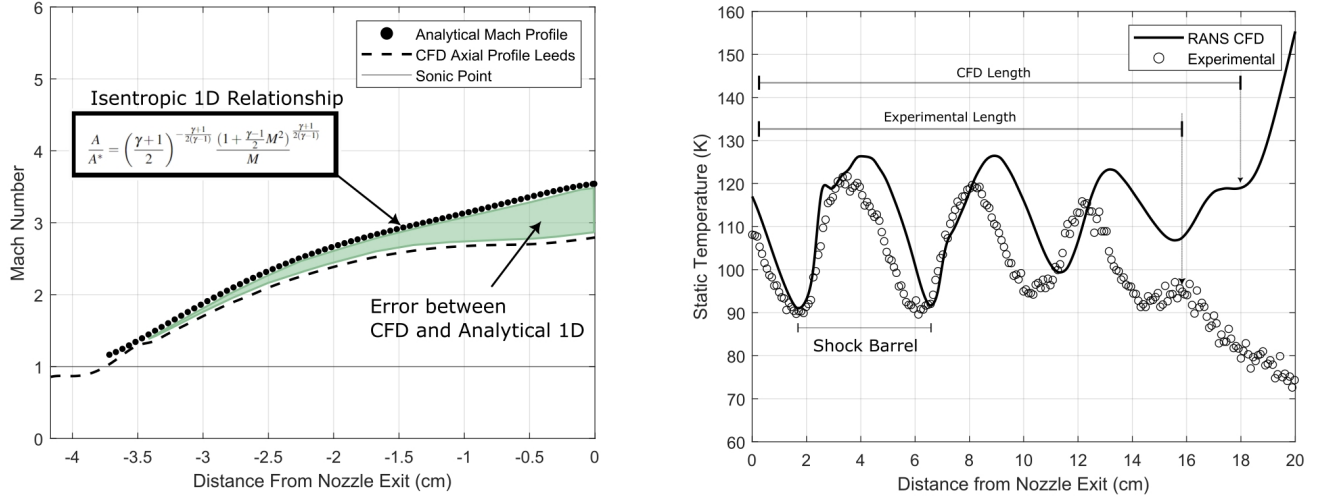
FIG. 12. 1D static temperature profile taken across the axis of the jet (left). comparison of analytical (Equation 3) and centerline Mach number from the CFD across the nozzle, where 0 mm is the nozzle inlet (right). These are the results from Nozzle 1 in the Leeds setup using nitrogen, P_{res} = 5222 Pa, P_{chm} = 170 Pa and $T_{res} = T_{chm}$ = 300 K. On the x-axis, 0 relates to the position of the nozzle exit, therefore negative values are inside the nozzle.

of the nozzle exit. There have been Large Eddy Simulations (LES) performed on Laval nozzles that show very good predictions in comparison to experiments[38,57]. although these are still slightly shifted and require excessive computation. Using LES does not allow the fast prototyping and simulation of supersonic nozzles that this study sets out.

As there is no experimental data inside the nozzle, the axial Mach profile in the nozzle region from the CFD was compared to Equation 3 from Section II A. The CFD and analytical Mach profiles follow closely at the entrance to the diverging section, although as the flow develops so does the boundary layer, and the analytical 1D isentropic relations does not capture this behaviour. It may also be because the inlet to the nozzle is coming in at a 90° angle to the flow axis, hence the discrepancies in Mach number profile across the nozzle. The average static pressure on the plane of the nozzle exit and the ambient static pressure in the CFD were found to be 163.8919 Pa and 163.8944 Pa respectively. Therefore, as discussed in Section II B, the flow is considered near optimal as $P_{exit} = P_{amb}$. The optimal conditions in the experiments (which are the results shown here) are also optimal in the CFD case. This again shows that the CFD model can accurately predict flow regimes, flow structure and global quantities of low-temperature, low-density supersonic jets.

A comparison of the main flow quantities between the experimental and CFD results can be seen in Table V. This shows the effectiveness of CFD in predicting the global flow quantities as they are within 6.4% and 4.9% for average temperature and Mach number respectively. The standard deviation of temperature and Mach number is within 10.3% and 15.3% respectively. Despite the large percentage difference, it is important to note that this is only a 1.1 K and 0.036 difference in the standard deviation of temperature and Mach number respectively.

The results in this section highlight that the use of a computationally inexpensive 2D axisymmetric model is appropriate and can be used as a predictive tool for low-temperature, low-density supersonic jet flows in the CRESU method.

2. Effect of Reservoir Size

As the reservoir size of Birmingham is ≈ 39 times larger in volume than Leeds, its effect was investigated using the same nozzle, bath gas and near identical reservoir and vacuum chamber conditions, which can be seen in Table II. The respective groups apparatus was used in each case. As both the reservoir and chamber sizes differ between the apparatuses, a test case was performed using CFD to ensure the vacuum chamber size had no impact on the results. Increasing the vacuum chamber size had a negligible impact on results, therefore this concludes that the reservoir is the main source of difference between both groups. Experimental and RANS studies were conducted using each setup with the conditions given in Table II, and the 1D temperature characterisation profile for the cases can be seen in Figure 14.

The experimental results from both groups show identical flow features, which are three main sinusoidal peaks, followed by a decrease in temperature once the flow has broken down. When using the large reservoir, the experimental results are shifted in front of the CFD, which could attributed to the displacement effect caused by the Pitot tube used to obtain the experimental results. Again like the case with the smaller reservoir, the magnitude of the shocks and shock barrels are being predicted accurately with the CFD model. A compari-
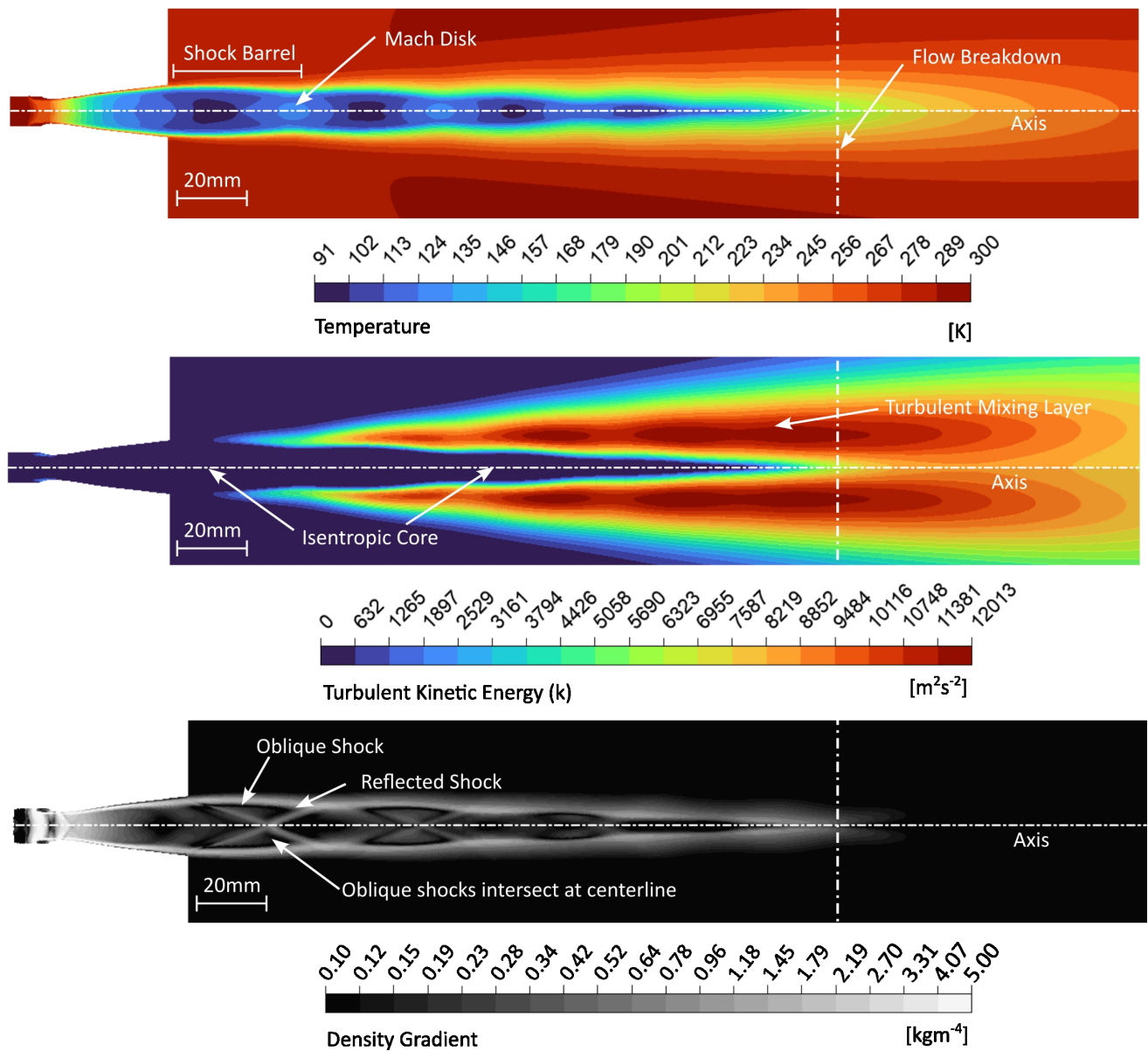
FIG. 13. Freestream CFD results for M2.25 Nozzle in the Leeds setup using Nitrogen, P_{res} = 5222 Pa, P_{chm} = 170 Pa and $T_{res} = T_{chm}$ = 300 K. Static Temperature contour with 20 contour bands (top). Turbulent kinetic energy contour with 20 colour bands showing isentropic core (blue) and mixing layer development (middle). Numerical schlieren plot calculated using density gradient with a log scale colourmap ranging from 0 to 5 (bottom) showing expansion and compression waves that propagate from the nozzle exit. The white dotted line represents the flow breakdown (stable flow length) for the supersonic jet.

son between the main flow parameters between the RANS and experimental using both apparatuses is shown in Table VI.

Increasing the reservoir size makes minimal difference to the magnitude of flow oscillation around the mean, but it makes a significant difference to the stable flow length. The stable flow length increases by 16.8% and 9.1% for the experimental and RANS CFD cases respectively when increasing the reservoir size. Having a larger reservoir causes the back pressure behind the supersonic nozzle to be more stable during a pulse as there is a larger buffer of gas during operation.

The larger reservoir also causes the flow to enter the nozzle at a much less steep angle as compared to the smaller reser-

voir. This reduces the turbulence generated inside the reservoir and nozzle inlet, which causes the mixing layer to develop slower, resulting in flow in a significantly more stable, longer flow as compared to the smaller reservoir. This reduction in turbulence may be why the CFD can predict the jet structure much more accurately for the Birmingham apparatus compared to the smaller reservoir used at Leeds.

It is also important to note that the optimal pressures for a specific nozzle does not change by much between groups using the same bath gas. The optimal reservoir and chamber pressure at Leeds is 5222.7 Pa and 170.7 Pa respectively whilst at Birmingham it was 5203.5 Pa and 169.7 Pa respec-
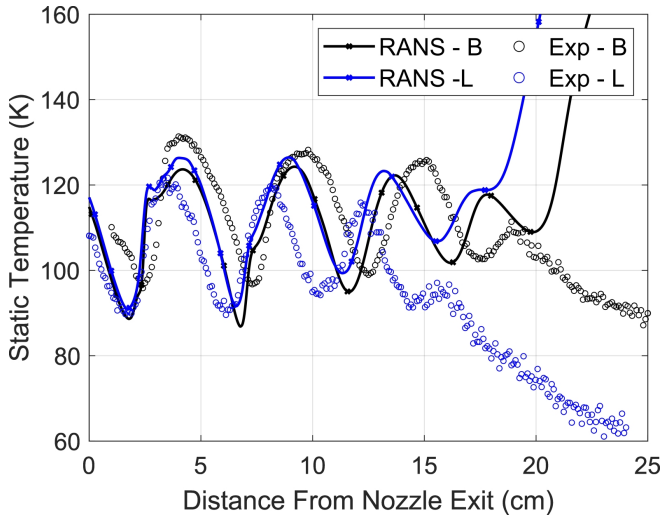
FIG. 14. 1D characterisation profile of axial static temperature for both RANS and experimental using the Nozzle 1 with the conditions given in Table III. L and B refers to the experimental and numerical results obtained from Leeds and Birmingham respectively.

TABLE VI. Comparisons of important flow quantities for experimental and RANS results using both Leeds and Birmingham's setup. The inlet conditions can be seen in table III, the turbulent intensity for all cases was 1%. Results show an average ± one standard deviation within the stable flow region across the flow axis. L and B denote results using Leeds or Birmingham setup respectively.

-	$T_{avg} \pm \sigma_T$ (K)	$M_{avg} \pm \sigma_M$	L_{flow} (cm)
Exp-L	104.5 ± 9.5	3.07 ± 0.24	15.9
RANS-L	111.6 ± 10.6	2.92 ± 0.20	18.0
Exp-B	113.4 ± 10.4	2.82 ± 0.21	19.1
RANS-B	109.7 ± 10.3	2.90 ± 0.23	19.8

tively. This is 0.3% difference in reservoir pressure and 0.58% in chamber pressure between both groups. This means that one nozzle and set of conditions can be used between groups with minimal impact on results, assuming the apparatuses are similar.

V. ACRE FRAMEWORK

To allow CFD characterisation of supersonic nozzles to be incorporated into the current design workflow for the CRESU method without disrupting current practice, a MATLAB package known as ACRE was developed guided by the information gained by studies carried out in this work. ACRE is open source and can be found at https://github.com/sc1dr/ACRE. It contains a user guide with all the necessary information to start using the framework. There are also additional supporting studies and various benchmark cases for comparison. It has been tested successfully on two different HPC systems at the University of Leeds and the University of Birmingham.

The ACRE framework, is an acronym that stands for "(A)utomated CFD (C)haracterisation for Low Temperature (Re)action Kinetics". ACRE was developed on MATLAB and can be deployed onto any Linux high performance computer (HPC) cluster with minimal effort. The toolbox allows any user to perform CFD on any supersonic nozzle profile (has to be axisymmetric) for the CRESU method (currently limited to $M < 5$) with no prior knowledge of CFD. ACRE automatically creates geometry, meshing and solution scripts for Ansys ICEM and Ansys Fluent as shown in Figure 15.
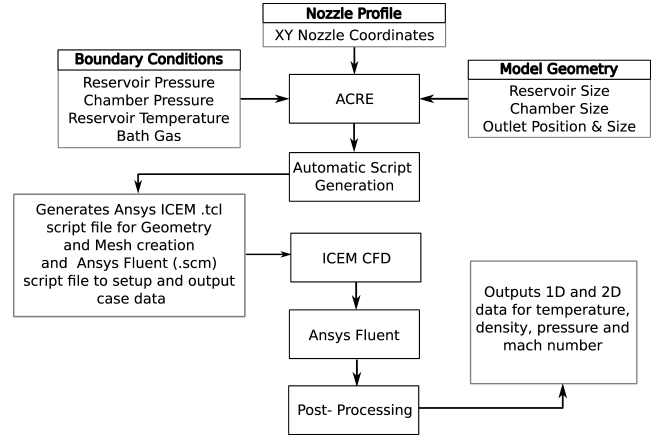

FIG. 15. High level workflow overview of the ACRE framework, providing information to how inputs are used to generate automatic scrips for the geometry, meshing and solution processes. XY nozzle coordinates are supplied via a text file.

The scripts are generated subject to a extensive list of user defined inputs. These include the 1D axisymmetric nozzle profile, reservoir pressure, chamber pressure, chamber size, reservoir size, outlet position, outlet diameter and bath gas (either nitrogen, helium or argon).

ACRE then uses these scripts to generate an appropriate mesh using Ansys ICEM. The number of elements in the mesh scales with the nozzle size and chamber size (larger nozzle or chamber results in more elements). Mesh adaption is used for each case, refining the boundary layer on walls where the y^+ value is < 1 for each case, ensuring boundary layer is resolved for each case that is run independent of the nozzle or Mach number. The Ansys Fluent script then sets up the case (the methodology is the same as section III B 4) using the generated mesh and runs until convergence is met. The results from the numerical simulation are then post-processed using MATLAB, and it provides the user with an easily readable data file containing 1D and 2D data for temperature, density, pressure and Mach number that can be used to characterise the nozzle with the specified inputs. The framework also allows a user to input one nozzle profile and parametrically vary the reservoir or the chamber pressure to improve the performance of the jet. A high-fidelity CFD simulation of Nozzle 1 for example takes $\approx$ 10-15 minutes for the entire workflow, including creation of geometry, meshing and solving, (depending on the pressure ratio, nozzle size and chamber geometry) using the ACRE framework on a 40-core 2.0 Ghz Xeon Gold 6138 CPU.

VI. APPLICATION OF FRAMEWORK TO OTHER NOZZLES

ACRE, as discussed in section III B, was used to compare the CFD results with existing experimental data. The numerical setup of the ACRE framework is identical to section III B. The reservoir pressure, chamber pressure, bath gas and nozzle used for comparison are seen in Table VII. The meshes used for each case were generated using the ACRE framework.

TABLE VII. Chamber pressure, reservoir pressure, bath gas, nozzle and setup used in both the experiments and CFD calculations. The experimental pressures have been averaged throughout the run. The setup type relates to the size of the chamber and reservoir as indicated in Table II. The nozzle name relates to sizing shown in Table I. NPR is the nozzle pressure ratio and is calculated by dividing the reservoir pressure by the chamber pressure. Note that different bath gasses can be used with the same nozzle to obtain a different temperature by changing the pressure conditions.

Run #	Nozzle	P_{res} (Pa)	P_{chm}(Pa)	NPR	Gas	Setup Type[a]
1	1	10600	198	53.5	N_2	L
2	1	10583	218	48.5	N_2	L
3	1	10530	243	43.3	N_2	L
4	1	10526	277	38.0	N_2	L
5	1	10592	314	33.7	N_2	L
6	2	11272	54	208.7	Ar	L
7	2	11250	56	200.9	Ar	L
8	2	11361	60	189.3	Ar	L
9	2	11317	63	179.6	Ar	L
10	2	11340	73	155.3	Ar	L
11	2	12314	86	143.2	He	L
12	2	12294	95	129.4	He	L
13	2	12280	104	108.1	He	L
14	2	12288	113	108.7	He	L
15	2	12251	123	99.6	He	L
16	2	6041	40	151.0	N_2	L
17	2	6017	41	146.8	N_2	L
18	2	6041	44	137.3	N_2	L
19	2	6027	47	128.2	N_2	L
20	2	6025	51	118.1	N_2	L
21	1	5237	129	40.7	N_2	B
22	1	5209	161	32.3	N_2	B
23	1	5260	173	30.5	N_2	B
24	1	5256	191	27.5	N_2	B
25	2	5521	29	190.4	N_2	B
26	2	5500	35	157.1	N_2	B
27	2	5514	37	149.0	N_2	B
28	2	5521	39	141.6	N_2	B

[a] Setup type of L and B refer to Leeds and Birmingham's reservoir and chamber setup respectively.

A wide range of bath gases and pressures were used to illustrate how robust the framework is in predicting experimental data. The results for each of the runs can be seen in Table VIII which contains the key quantities for both the RANS CFD cases and experimental data. In this the flow properties, such as average Mach number and temperature are evaluated across the stable region of the supersonic jet (where chemical kinetics are performed in the laboratory). A graphical comparison

between experimental and RANS results for some of the cases shown can be found in supplementary material.

The disparity between the RANS and experimental results is greater when away from the optimal design conditions (indicated in Table VIII by the bold rows). In the sub optimal cases, where the standard deviation of temperature is high, the flow is either over-expanded or under-expanded. This is because away from optimal pressure conditions, the CFD predicts strong shockwave structures, which cause the average temperature to be much higher in comparison to the experimental results. The CFD captures the length of the flow seen in the experiments very accurately, for example in runs 1-5, the error between ranges from 1-3 cm. The flow length for cases 6-20 have not been included as the Pitot tube translation stage at Leeds can only be used up to 30cm from the nozzle exit, therefore the flow length could not be obtained. This is also done for the Birmingham cases as it is relatively hard to find the exact flow length as there is not a distinct breakdown point as the Rayleigh-Pitot equations fail to do so. The predictions of the RANS cases carried out using Birmingham's apparatus is much closer to experimental results. Runs 21-24 with nitrogen show that the average temperature and standard deviation of temperature is within 5K. This is because the Birmingham apparatus has a much larger reservoir, and the CFD model is more accurately capturing the state of the reservoir as compared to the Leeds runs with the smaller reservoir. Again as discussed before, the length of the stable jet is much longer when using larger reservoir, and this is seen across all cases with Nozzle 1 when comparing Runs 21-24 with Runs 1-5 as they both operate at similar pressure ratios.

Although the CFD is over predicting average temperature and standard deviation of temperature across the stable jet for the majority of cases using both the Leeds and Birmingham setups, the CFD is accurately predicting the trends seen in the experimental results when changing the nozzle shape, reservoir pressure, chamber pressure and bath gas. This can be seen as the increase in average temperature, average Mach number, standard deviations of temperature and Mach number, and flow length are proportional to the rise in NPR throughout all the runs for the experimental results.

The runs 1-5 in Table VIII show that the average temperature in the CFD increases from 99.9 K to 108.4 K when decreasing the NPR from 53.5 to 33.7, which is an increase by 8.5 K. A similar trend is shown in runs 1-5 in the experimental data when decreasing the NPR, and the average temperature increases by 14 K. In runs 6-10, increasing the NPR from 54 to 73 increases the average temperature by 5.8 K in the CFD, while the average temperature increases by 1.9 K in the experiments. The disparity between the RANS CFD and experiments for average temperature seen across the runs with nitrogen is generally 5-10 K across all nozzles used, For helium and argon, its slightly larger with an average temperature error of $\approx$ 10-15 K. The difference between the nitrogen cases and helium/argon may also be attributed to the larger pressure ratios (3-4 times larger) and much lower average jet temperatures that are being generated when using these bath gasses with the same nozzle.

The optimal chamber and reservoir pressure for a particu-

TABLE VIII. Comparison of main flow parameters of both RANS CFD and experimental data, the runs correspond to data shown in Table VII. L_{flow} is the stable flow length, some experimental lengths are denoted with '-' as the Pitot tube movement is restricted to 30 cm away from the nozzle exit at Leeds. The temperature and Mach number values shown are the mean temperature and one standard deviation across the stable flow length for both experiments and numerical simulations. Rows in bold relate to the optimal case in each set of pressure conditions used with a specific nozzle and bath gas. It is important to note that the pressure conditions that generate the lowest σ_T for each nozzle is used in the kinetic studies. Off design conditions are included to show that the CFD can be used to predict a wide range of flow conditions.

Run #	RANS CFD			Experimental		
	$T_{avg} \pm \sigma_T$ (K)	$M_{avg} \pm \sigma_M$	L_{flow} (cm)	$T_{avg} \pm \sigma_T$ (K)	$M_{avg} \pm \sigma_M$	L_{flow} (cm)
1	99.9 ± 20.1	3.24 ± 0.56	21.8	83.7 ± 12.9	3.62 ± 0.39	20.1
2	100.9 ± 17.5	3.20 ± 0.47	20.7	87.0 ± 11.7	3.51 ± 0.33	18.4
3	102.3 ± 14.6	3.15 ± 0.37	19.2	90.6 ± 10.8	3.41 ± 0.29	16.7
4	105.2 ± 12.3	3.07 ± 0.28	17.7	93.9 ± 10.2	3.31 ± 0.26	14.9
5	**108.4 ± 11.5**	**3.00 ± 0.26**	**16.2**	**97.7 ± 9.4**	**3.21 ± 0.23**	**13.0**
6	**39.7 ± 7.5**	**4.55 ± 0.47**	**40.2**	**28.7 ± 2.7**	**5.33 ± 0.27**	**−**
7	40.4 ± 8.3	4.51 ± 0.51	39.4	29.1 ± 3.1	5.29 ± 0.31	-
8	41.3 ± 9.2	4.47 ± 0.56	38.6	29.4 ± 3.6	5.26 ± 0.34	-
9	42.3 ± 10.3	4.43 ± 0.60	37.4	30.3 ± 4.8	5.20 ± 0.43	-
10	45.5 ± 13.1	4.28 ± 0.71	34.6	30.6 ± 5.2	5.16 ± 0.45	-
11	**43.7 ± 5.3**	**4.22 ± 0.28**	**41.4**	**34.1 ± 3.6**	**4.83 ± 0.27**	**−**
12	45.5 ± 7.1	4.14 ± 0.36	39.3	34.7 ± 4.2	4.80 ± 0.31	-
13	47.1 ± 8.6	4.07 ± 0.43	37.3	35.4 ± 5.0	4.74 ± 0.36	-
14	48.9 ± 10.3	4.00 ± 0.50	35.5	36.1 ± 5.6	4.70 ± 0.38	-
15	51.3 ± 12.2	3.90 ± 0.57	33.7	36.8 ± 6.4	4.66 ± 0.43	-
16	74.5 ± 2.6	3.90 ± 0.092	38.0	66.5 ± 2.1	4.18 ± 0.087	-
17	**75.0 ± 2.6**	**3.88 ± 0.090**	**37.6**	**67.2 ± 1.9**	**4.15 ± 0.078**	**−**
18	76.0 ± 3.0	3.85 ± 0.10	36.6	68.0 ± 2.3	4.11 ± 0.090	-
19	77.4 ± 4.2	3.80 ± 0.13	35.2	59.2 ± 3.4	4.07 ± 0.13	-
20	79.0 ± 5.7	3.76 ± 0.18	34.0	70.6 ± 4.5	4.02 ± 0.16	-
21	102.7 ± 14.9	3.08 ± 0.38	23.4	101.6 ± 12.7	3.09 ± 0.30	23.0
22	108.3 ± 10.6	2.93 ± 0.23	20.9	109.1 ± 9.9	2.91 ± 0.21	20.0
23	**110.1 ± 10.3**	**2.90 ± 0.22**	**20.1**	**110.3 ± 7.4**	**2.88 ± 0.15**	**19.0**
24	113.5 ± 10.9	2.82 ± 0.23	17.7	112.4 ± 8.8	2.84 ± 0.18	18.9
25	70.5 ± 4.3	3.99 ± 0.17	47.9	64.9 ± 8.1	4.18 ± 0.35	-
26	72.9 ± 2.6	3.90 ± 0.095	44.9	69.8 ± 5.0	4.00 ± 0.20	-
27	74.0 ± 2.4	3.86 ± 0.085	43.7	70.9 ± 3.8	3.96 ± 0.14	-
28	**74.8 ± 2.8**	**3.83 ± 0.093**	**42.7**	**71.4 ± 2.9**	**3.94 ± 0.11**	**−**

lar nozzle and bath gas is the same in both the experimental and CFD results, with the exact conditions shown in bold in Table VIII. The optimal jet used for kinetic studies is defined as the jet with the lowest value for σ_T. The pressure conditions that produce a non-optimal jet are discarded and not used in kinetic studies. A comparison between the optimal experimental and numerical runs for T_{avg} and σ_T is shown in Figure 16. The average temperature of the jet is predicted extremely well by the computational model, and the correlation $R^2 = 0.99$. The linear fit equation of the data is $y = 1.07x$ through the origin, which shows that the average temperature of the experiments can be predicted with the computational model to within 7% over the range of average jet temperatures analysed in this study. The standard deviation of temperature is captured well, with the linear trend line being $y = 1.35x$, and the correlation $R^2 = 0.95$, therefore the predictions by the computational model are within 35%. It is important to note that this percentage is high as the values of σ_T are small, and the computational predictions of the optimal runs vary on average 2.1 K from the experimental results.

The data generated using the ACRE framework shows that

the CFD is able to accurately predict supersonic jet structures and the global flow quantities of interest for chemical kinetic studies, such as the T_{avg}, σ_T and L_{flow} from the experimental runs. Therefore CFD can be used to infer how good a particular nozzle, bath gas and pressure condition is without the need for experimental measurement. The ACRE framework can be used to predict values for T_{avg} and σ_T for any nozzle profile, bath gas and operating that generates a supersonic jet under Mach 5. The ACRE framework can also readily be used to determine optimal pressure conditions for any nozzle and bath gas combination accurately as shown in Table VIII. The framework could effectively replace the need for the time consuming pressure optimisation that is routinely carried out experimentally to find the best conditions for a particular nozzle. As the ACRE framework allows the input of any nozzle profile, it can be used to test nozzles that are designed using the existing MOC method. The input parameters set in the MOC program could be parametrically investigated to find out the best settings to produce the most optimal nozzle for a range of temperatures. This shows that ACRE can be used as a powerful tool to aid flow characterisation and supersonic

nozzle design for low temperature kinetics.

VII. CONCLUSIONS & FUTURE WORK

In conclusion, a robust CFD model has been developed to overcome the issues with the frequently used MOC, giving insight into supersonic wake structures and global jet quantities, such as average temperature, standard deviation of temperature and flow length for low temperature, low pressure supersonic jets used in kinetic studies. This has been used to capture the flow characteristics of low temperature jets in far more detail than previously reported.

The computational model has been validated against two different experimental apparatus at the University of Leeds and the University of Birmingham. With the benchmark nozzle, the computational model predicted the experimental average jet temperature within 7.1 K and 3.7 K, the standard deviation of temperature within 1.1 K and 0.1 K and the stable flow length within 2.1 cm and 0.7 cm for the Leeds and Birmingham apparatus respectively.

The CFD model has also been used to explore additional observations of the experimental approach. Adding a Pitot tube into the supersonic jet, as is often done during flow characterisation, disrupts the flow field and causes a bow shock to form on the leading edge of the Pitot tube. The bow shock causes a shift in the temperature profile as compared to the jet with no Pitot tube (e.g., when kinetic experiments are carried out). The extent of the Pitot tube effect, using Nozzle 1 in the Leeds apparatus with nitrogen and its optimal pressure conditions were analysed numerically. This study showed that the temperature profile was shifted away from the nozzle exit by 2-3 mm and the Pitot results were within 1.5 K of the freestream results for average temperature. This demonstrates that the blockage effect of the Pitot tube is negligible.

The experimental apparatus at the University of Birmingham has a pre-expansion reservoir that is 39 times larger than the one used at Leeds. Groups worldwide use a variety of different-sized reservoirs, for example, they can range from 0.78 cm^3 at Leeds to 22,500 cm^3 at the University of Rennes. CFD studies demonstrated that for small reservoirs, pulsing of the high pressure gas generates high turbulence inside the reservoir, causing the turbulent mixing layer surrounding the isentropic core to develop significantly quicker, reducing stable flow length. Under similar conditions the larger reservoir studied here gave an increase in stable jet length of $\approx$17% (experiment) and 9% (CFD). However, larger reservoirs require larger vacuum pumps and more gas per pulse, and there is inevitably a trade-off. This also demonstrates that steady-state models, which are computationally cheaper to run, offer useful predictive capabilities across a range of equipment designs.

Finally, A MATLAB framework named ACRE ("Automated Characterisation for Low Temperature Reaction Kinetics") has been developed to allow researchers to rapidly prototype supersonic nozzles and obtain optimal pressure conditions before manufacturing and experimental testing. The framework has been validated with a variety of different nozzles and conditions. It can be found at https://github.com/sc1dr/ACRE. The ACRE framework can predict the performance of supersonic jets generated using Laval nozzles within 5-10 K for both average temperature and standard deviation in temperature across a wide range of operating conditions, nozzles and bath gases. It provides a way of using CFD tools, with the advantages they bring, to the wider community. Automated simulation protocols such as this also open the possibility of design optimisation, for example to establish the optimal jet profile for a specified jet temperature with the lowest possible σ_T, thereby ensuring the greatest robustness of the kinetics study.

SUPPLEMENTARY MATERIAL

The supplementary material contains (i) additional information on the experimental apparatus, including pictures of the Leeds apparatus and Pitot tubes (ii) mesh dependence studies for Nozzle 2 and the numerical Pitot tube study (iii) computational studies used to guide the computational model, such as comparing the density and pressure-based solver and (iv) graphical comparisons of the results obtained using the computational framework with experimental data.

DATA AVAILABILITY STATEMENT

The data that support the findings of this study are available from the corresponding author upon reasonable request

REFERENCES

[1] A. G. G. M. Tielens, "The molecular universe," Rev. Mod. Phys. **85**, 1021–1081 (2013).

[2] A. Potapov, A. Canosa, E. Jiménez, and B. Rowe, "Uniform supersonic chemical reactors: 30 years of astrochemical history and future challenges," Angewandte Chemie International Edition **56**, 8618–8640 (2017).
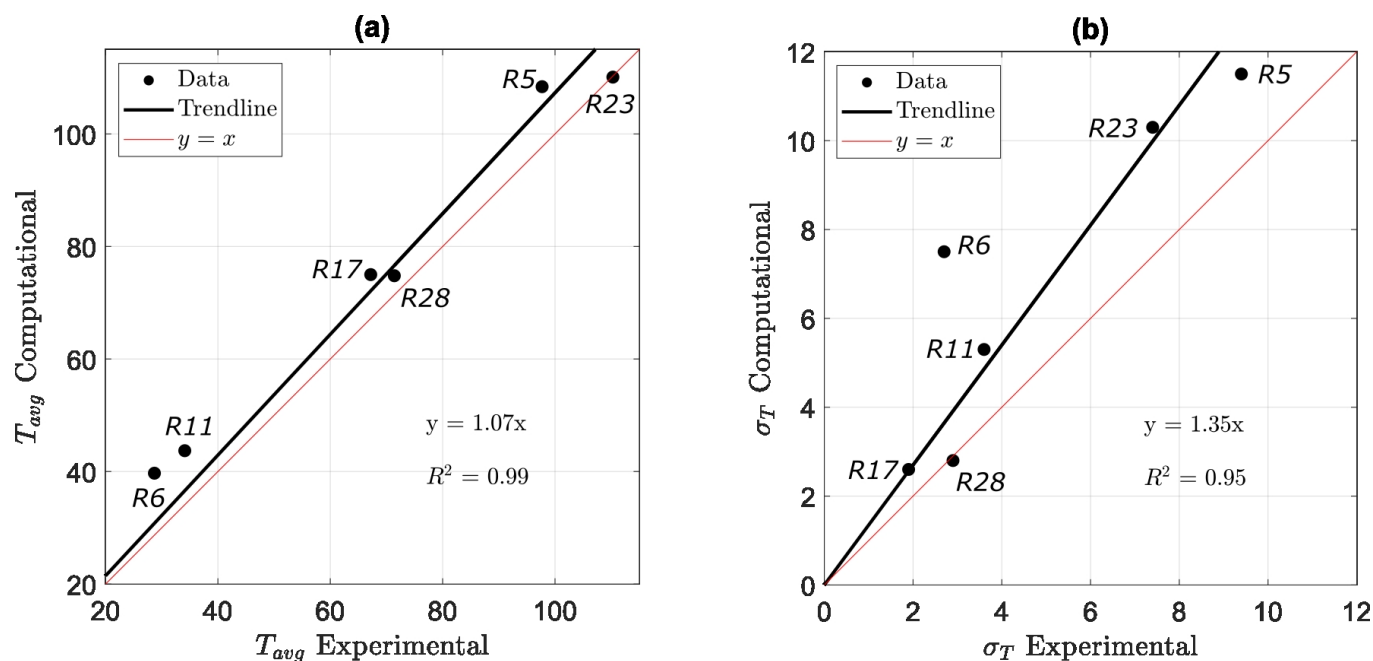
FIG. 16. Comparison of experimental and numerical results for T_{avg} (a) and σ_T (b). Data points are taken from the bold rows in Table VIII. Both plots have a linear trend line that crosses the origin, and the corresponding equation and R^2 value is embedded. The red line indicates $y = x$, this is where a perfect prediction by the computational model would be. The data points are labelled with respect to the run number shown in Table VII, for example R12 means results from run 12.

[3]E. Herbst, "Chemistry in the interstellar medium," Annual Review of Physical Chemistry **46**, 27–54 (1995).

[4]D. E. Heard, "Rapid acceleration of hydrogen atom abstraction reactions of oh at very low temperatures through weakly bound complexes and tunneling," Accounts of Chemical Research **51**, 2620–2627 (2018).

[5]P. Thaddeus, "The prebiotic molecules observed in the interstellar gas," Philosophical Transactions of the Royal Society B: Biological Sciences **361**, 1681–1687 (2006).

[6]I. Jiménez-Serra, J. Martín-Pintado, A. Insausti, E. R. Alonso, E. J. Cocinero, and T. L. Bourke, "The ska as a prebiotic molecule detector," Frontiers in Astronomy and Space Sciences **9** (2022), 10.3389/fspas.2022.843766.

[7]B. Jolland, N. Jamai-Eddine, D. Papanastasiou, A. Lekkas, S. Carles, and L. Biennier, "A mass-selective ion transfer line coupled with a uniform supersonic flow for studying ion-molecule reactions at low temperatures," Journal of Chemical Physics **150** (2019), 10.1063/1.5086386.

[8]S. E. Taylor, A. Goddard, M. A. Blitz, P. A. Cleary, and D. E. Heard, "Pulsed laval nozzle study of the kinetics of OH with unsaturated hydrocarbons at very low temperatures," Physical Chemistry Chemical Physics **10**, 422–437 (2008).

[9]A. Canosa, A. J. Ocaña, M. Antiñolo, B. Ballesteros, E. Jiménez, and J. Albaladejo, "Design and testing of temperature tunable de laval nozzles for applications in gas-phase reaction kinetics," Experiments in Fluids **57** (2016), 10.1007/s00348-016-2238-1.

[10]D. B. Atkinson and M. A. Smith, "Design and characterization of pulsed uniform supersonic expansions for chemical applications," Review of Scientific Instruments **66**, 4434–4446 (1995).

[11]D. B. Atkinson and M. A. Smith, "Radical-molecule kinetics in pulsed uniform supersonic flows: Termolecular association of OH + NO between 90 and 220 k," The Journal of Physical Chemistry **98**, 5797–5800 (1994).

[12]E. Jiménez, B. Ballesteros, A. Canosa, T. M. Townsend, F. J. Maigler, V. Napal, B. R. Rowe, and J. Albaladejo, "Development of a pulsed uniform supersonic gas expansion system based on an aerodynamic chopper for gas phase reaction kinetic studies at ultra-low temperatures," Review of Scientific Instruments **86** (2015), 10.1063/1.4918529.

[13]G. Dupeyrat, J. B. Marquette, and B. R. Rowe, "Design and testing of axisymmetric nozzles for ion-molecule reaction studies between 20 °K and 160 °K," The Physics of Fluids **28**, 1273–1279 (1985).

[14]O. Abdelkader Khedaoui, *Improving the sensitivity of mm-wave rotational spectroscopy in uniform supersonic flows for laboratory astrophysics applications*, Ph.D. thesis, Université de Rennes (2022).

[15]B. R. Rowe, G. Dupeyrat, J. B. Marquette, and P. Gaucherel, "Study of the reactions $N_2^+ + 2N_2 \rightarrow N_4^+ + N_2$ and $O_2^+ + 2O_2 \rightarrow O_4^+ + O_2$ from 20 to 160 k by the cresu technique," The Journal of Chemical Physics **80**, 4915–4921 (1984).

[16]R. Sánchez-González, R. Srinivasan, J. Hofferth, D. Y. Kim, A. J. Tindall, R. D. Bowersox, and S. W. North, "Repetitively pulsed hypersonic flow apparatus for diagnostic development," AIAA Journal **50**, 691–697 (2012).

[17]C. Berteloite, M. Lara, A. Bergeat, S. D. Le Picard, F. Dayou, K. M. Hickson, A. Canosa, C. Naulin, J.-M. Launay, I. R. Sims, and M. Costes, "Kinetics and dynamics of the $S(^1D_2) + H_2 \rightarrow SH + H$ reaction at very low temperatures and collision energies," Phys. Rev. Lett. **105**, 203201 (2010).

[18]O. Durif, "Design of de laval nozzles for gas-phase molecular studies in uniform supersonic flow," Physics of Fluids **34** (2022), 10.1063/5.0060362.

[19]B. R. Rowe, A. Canosa, and D. E. Heard, *Uniform Supersonic Flows in Chemical Physics* (WORLD SCIENTIFIC (EUROPE), 2022).

[20]R. J. Shannon, *Experimental and computational studies of hydroxyl radical kinetics at very low temperatures*, Ph.D. thesis, University of Leeds (2012).

[21]R. L. Caravan, *Low Temperature Kinetic Studies using a Pulsed Laval Nozzle Apparatus*, Ph.D. thesis, University of Leeds (2015).

[22]J. P. Messinger, D. Gupta, I. R. Cooke, M. Okumura, and I. R. Sims, "Rate constants of the CN + toluene reaction from 15 to 294 k and interstellar implications," Journal of Physical Chemistry A **124**, 7950–7958 (2020).

[23]A. J. Ocaña, S. Blázquez, A. Potapov, B. Ballesteros, A. Canosa, M. Antiñolo, L. Vereecken, J. Albaladejo, and E. Jiménez, "Gas-phase reactivity of CH_3OH toward OH at interstellar temperatures (11.7-177.5 k): Experimental and theoretical study," Physical Chemistry Chemical Physics **21**, 6942–6957 (2019).

[24]A. Mortada, "Ion-molecule reactions at low temperature with uniform supersonic flows and insights into the chemistry of astrophysical environments," (2022).

[25] N. Suas-David, S. Thawoos, and A. G. Suits, "A uniform flow-cavity ring-down spectrometer (uf-crds): A new setup for spectroscopy and kinetics at low temperature," Journal of Chemical Physics **151** (2019), 10.1063/1.5125574.

[26] S. G. Mironov, V. M. Aniskin, T. A. Korotaeva, and I. S. Tsyryulnikov, "Effect of the pitot tube on measurements in supersonic axisymmetric underexpanded microjets," Micromachines **10** (2019), 10.3390/mi10040235.

[27] H. G. B and L. G, "The displacement effect of pitot tube in narrow wake at subsonic and supersonic speeds," (1956).

[28] X. Zhang, P. Hao, and Z. Yao, "The measurement error analysis when a pitot probe is used in supersonic air flow," Science China: Physics, Mechanics and Astronomy **54**, 690–696 (2011).

[29] A. Balabel, A. M. Hegab, M. Nasr, and S. M. El-Behery, "Assessment of turbulence modeling for gas flow in two-dimensional convergent-divergent rocket nozzle," Applied Mathematical Modelling **35**, 3408–3422 (2011).

[30] S. L. B. T. Masgo, "Evaluation of turbulence models for the air flow in a planar nozzle," Ingenius **2019**, 25–37 (2019).

[31] M. Abedi, R. Askari, J. Sepahi-Younsi, and M. R. Soltani, "Axisymmetric and three-dimensional flow simulation of a mixed compression supersonic air inlet," Propulsion and Power Research **9**, 51–61 (2020).

[32] G. Besagni and F. Inzoli, "Computational fluid-dynamics modeling of supersonic ejectors: Screening of turbulence modeling approaches," Applied Thermal Engineering **117**, 122–144 (2017).

[33] M. A K and T. Sunny, "Design of a double parabolic supersonic nozzle and performance evaluation by experimental and numerical methods," Aircraft Engineering and Aerospace Technology **91** (2018), 10.1108/AEAT-12-2017-0275.

[34] X. Lian, H. Xu, L. Duan, and T. Sun, "Flow structure and parameter evaluation of conical convergent–divergent nozzle supersonic jet flows," Physics of Fluids **35** (2023), 10.1063/5.0151556.

[35] S. Croquer, S. Poncet, and Z. Aidoun, "Turbulence modeling of a single-phase r134a supersonic ejector. part 1: Numerical benchmark," International Journal of Refrigeration **61**, 140–152 (2016).

[36] F. Liu, D. Sun, R. Zhu, and Y. Li, "Characteristics of flow field for supersonic oxygen multijets with various laval nozzle structures," Metallurgical and Materials Transactions B **50** (2019), 10.1007/s11663-019-01652-7.

[37] Y. Liao and D. Lucas, "3d cfd simulation of flashing flows in a converging-diverging nozzle," Nuclear Engineering and Design **292**, 149–163 (2015).

[38] D. Munday, E. Gutmark, J. Liu, and K. Kailasanath, "Flow structure and acoustics of supersonic jets from conical convergent-divergent nozzles," Physics of Fluids **23**, 116102 (2011).

[39] S. Thawoos, N. Suas-David, R. M. Gurusinghe, M. Edlin, A. Behzadfar, J. Lang, and A. G. Suits, "Low temperature reaction kinetics inside an extended Laval nozzle: REMPI characterization and detection by broadband rotational spectroscopy," The Journal of Chemical Physics **159**, 214201 (2023).

[40] B. Schläppi, J. H. Litman, J. J. Ferreiro, D. Stapfer, and R. Signorell, "A pulsed uniform laval expansion coupled with single photon ionization and mass spectrometric detection for the study of large molecular aggregates," Physical Chemistry Chemical Physics **17**, 25761–25771 (2015).

[41] P. H. Oosthuizen and W. E. Carscallen, *Introduction to Compressible Fluid Flow Introduction to*, 2nd ed., edited by A. J. Ghajar (Taylor Francis Group, 2014).

[42] S. Khare and U. Saha, "Rocket nozzles: 75 years of research and development," Sadhana **46** (2021).

[43] J. Anderson, *Modern Compressible Flow: With Historical Perspective*, Aeronautical and Aerospace Engineering Series (McGraw-Hill Education, 2003).

[44] P. M. Sforza, "Chapter 5 - nozzles," in *Theory of Aerospace Propulsion*, Aerospace Engineering, edited by P. M. Sforza (Butterworth-Heinemann, Boston, 2012) pp. 161–198.

[45] R. Baidya, A. Pesyridis, and M. Cooper, "Ramjet nozzle analysis for transport aircraft configuration for sustained hypersonic flight," Applied Sciences **8**, 574 (2018).

[46] M. Kiyak and O. Çakır, "Examination of machining parameters on surface roughness in edm of tool steel," Journal of Materials Processing Technology **191**, 141–144 (2007), advances in Materials and Processing Technologies, July 30th - August 3rd 2006, Las Vegas, Nevada.

[47] D. I. Lucas, T. Guillaume, D. E. Heard, and J. H. Lehman, "Highly instrumented low temperature reaction chamber (hiltrac): Design and implementation," (2024), manuscript in preparation.

[48] S. Colin, "Rarefaction and compressibility effects on steady or transient gas flows in microchannels," Microfluidics and Nanofluidics **1**, 268–279 (2005).

[49] A. Favre, *The Equations of Compressible Turbulent Gasses.* (Defense Technical Information Center, 1965).

[50] F. R. Menter, "Alaa 93-2906 zonal two equation k-cl, turbulence models for aerodynamic flows," (1993).

[51] D. C. Wilcox, *Turbulence modeling for CFD* (DCW Industries, 2006) p. 522.

[52] D. C. Wilcox, "Formulation of the k- turbulence model revisited," AIAA Journal **46**, 2823–2838 (2008).

[53] B. E. Launder and D. B. Spalding, "The numerical computation of turbulent flows," Computer Methods in Aplied Mechanics and Engineering **3**, 269–289 (1974).

[54] S. A. E. Miller and J. Veltin, "Experimental and numerical investigation of flow properties of supersonic helium-air jets," (2015).

[55] F. G. Schmitt, "About boussinesq's turbulent viscosity hypothesis: historical remarks and a direct evaluation of its validity," **335**, 617–627 (2007).

[56] P. J. Roache, "Quantification of uncertainty in computational fluid dynamics," (1997).

[57] J. Liu, K. Kailasanath, R. Ramamurti, D. Munday, E. Gutmark, and R. Lohner, "Large-eddy simulations of a supersonic jet and its near-field acoustic properties," AIAA Journal **47**, 1849–1865 (2009).